UNIVERSIDADE D
COIMBRA

João Pedro Gomes de Oliveira Braz

TRANS-A_2B-CORROLES ARE SUPERIOR PHOTOSENSITIZERS FOR LUNG CANCER

Dissertação no âmbito do Mestrado em Investigação Biomédica, no ramo de especialização em Oncobiologia, orientada pela Professora Doutora Maria Filomena Rabaça Roque Botelho, coorientada pela Doutora Susana Margarida Martins Lopes, e apresentada à Faculdade de Medicina da Universidade de Coimbra.

Outubro de 2020

Agradecimentos

Primeiramente, agradeço à minha orientadora, Professora Filomena Botelho, por me ter aceite no seu laboratório, pela partilha de conhecimento e pela inspiração que foi para mim. Foi sem dúvida um privilégio ser orientado por si. Espero um dia ter o seu gosto pela investigação, e a sua mestria na partilha de conhecimento.

À minha coorientadora, Doutora Susana Lopes, pela constante disponibilidade, pelas correções e conselhos, e por me ter ensinado tudo o que aprendi ao longo deste ano intenso no laboratório de Química Orgânica. Graças a si, posso dizer que para além do enorme gosto pela Química Orgânica teórica, desenvolvi um gosto ainda mais especial pela parte laboratorial desta área da ciência.

À Doutora Mafalda Laranjo, pela sua acessibilidade, entrega e dinamismo. Foi uma peça fundamental ao longo deste percurso, não só por todas as correções e conselhos, mas pelo seu perfeccionismo e otimismo, que me desafiou todos os dias a fazer mais e melhor sem nunca me deixar afetar por resultados menos positivos.

À Professora Marta Piñeiro, por ter sido sempre incansável, não só durante a tese, mas durante todo o meu percurso académico. A si lhe devo a paixão pela Química Orgânica, que alimentou uma constante aproximação do meu percurso académico à área da síntese orgânica e desenvolvimento de fármacos, e resultou neste projeto multidisciplinar do qual tanto me orgulho. Por todo o apoio, conselhos e boa disposição, o meu sincero obrigado.

À Professora Teresa Pinho e Melo, por me ter aceite no seu laboratório, e confiado este projeto. Agradeço ainda toda a preocupação que demonstrou ao longo de todo o projeto e todo o seu entusiasmo que sempre me motivou a superar os inúmeros obstáculos que me surgiram.

A todos os meus colegas do grupo da Biofísica e do grupo de Química Orgânica por toda a disponibilidade.

Aos meus amigos de sempre, Manuel, Elsa, Filipa, Grilo, Sara, Rente, Patrício, Fábio, Xana, Juliana, Rosa, Micas, Biscaia, Cristina, Mafalda, e a tantos outros por estarem sempre presentes quando mais precisei.

À Quantunna, em especial aos meus afilhados e aos meus (melhores) padrinhos por terem feito destes os melhores anos. Desde os ensaios de segundas e quintas, passando pelos Oito Badaladas, aos metros de finos sempre cantados. Vivi, vivo, e viverei Coimbra.

Ao meu grupo de fados Elegia, que apesar dos altos e baixos, me deu ensinamentos que guardarei para a vida.

À minha família, em especial aos meus pais, por todo o apoio que sempre me deram. São um exemplo dedicação, e a fonte inesgotável de amor e afeto. Obrigado por todos os sacrifícios, esta conquista é uma conquista nossa.

Finalmente, e não menos importante, um obrigado à minha avó, minha segunda mãe, que me viu começar este projeto e que, esteja onde estiver, se orgulha por me ver terminar. Para ti, pelo teu riso e pelos nossos fados de Coimbra, amo-te.

"Nas minhas veias corre um mar
De saudade e vontade de aqui voltar
Na maré cheia vai extravasar
Minhas lágrimas são salgadas por te amar.

É hora, meu amor de me ir embora
Ficas sempre na memória
De quem mais sorriu por ti
O que vivi…"

Abstract

Corroles are ring-contracted tetrapyrrolic macrocycles of the porphyrin family. Over the last decades, these smaller analogues of porphyrin have received much attention in the field of antitumor drugs development, particularly as photosensitizers (PS) in photodynamic therapy (PDT). PDT consists of a light-activated chemical reaction used to selectively destroy tissues, through the generation of singlet oxygen and other reactive oxygen species (ROS).

The Organic Chemistry research group of the University of Coimbra had previously reported the synthesis of a new type of *trans*-A_2B-corroles containing an oxime moiety. In this context, the project focused on the design and chemical synthesis of new corroles, and on *in vitro* evaluation of its potential use as PS in PDT of lung cancer.

In **Part A** of this work, three new compounds from this new chemical library of corroles were synthetized. This was achieved via two consecutive hetero-Diels-Alder reactions or conjugated additions of nitrosoalkenes, generated *in situ* from dehydrohalogetion of α,α-dihalo-oximes, with dipyrromethanes, followed by oxidative macro-cyclization with 2,3-dichloro-5,6-dicyano-1,4-benzoquinone (DDQ). The PS were characterized by ^{1}H NMR, ^{13}C NMR, ^{19}F NMR, and mass spectrometry. Then, its photophysical characterization was performed together with corroles previously synthesized in the Organic Chemistry Group.

In **Part B**, *in vitro* studies of these corroles based PDT were carried out in lung cancer cell lines. For that, the PS were solubilized in dimethylsulfoxide (DMSO) and administrated to A549 and H1299 cell lines in different concentrations ranged from 50 nM to 10 μM. Then, cells were incubated for 24 hours, and two different experiences were performed, in order to test photocytotoxicity and cytotoxicity. For photocytotoxicity assays, the cultures were washed with PBS, irradiated with a photon flux of 7.5 mW/cm^2, to a total of 10 J, and incubated for 24 hours before MTT and SRB assays. For cytotoxicity assays, the cultures were washed with PBS and incubated for 24 hours before MTT and SRB assays.

The preliminary MTT assays of some of these PS showed that, when under irradiation, the concentration value for the 50% inhibition of the metabolic activity (IC_{50}) was in the nanomolar range: 270 nM on H1299 and 127 nM on A549. SRB assays corroborate the results previously described. In fact, IC_{50} values were similar to those of other clinical approved PDT drugs, such as Foscan®. Furthermore, all corroles showed no dark citotoxicity in both cell lines.

Trans-A_2B-corrole's high photocytotoxicity and non-cytotoxicity corroborates its applicability as PS in PDT, pointing to a promising therapeutic effect, and support further studies.

Keywords:

Photodynamic therapy, corroles, *trans*-A_2B-corroles, lung cancer, photocytotoxicity.

Resumo

Corróis são macrociclos tetrapirrólicos em anel contraído da família das porfirinas. Nas últimas décadas, esses análogos mais pequenos da porfirina têm recebido muita atenção no campo do desenvolvimento de fármacos antitumorais, principalmente como fotossensibilizadores (PS) na terapia fotodinâmica (PDT). A PDT consiste numa reação química ativada pela luz usada para destruir seletivamente os tecidos, por meio da geração de oxigênio singleto e outras espécies reativas de oxigênio (ROS).

O grupo de investigação de Química Orgânica da Universidade de Coimbra já havia relatado a síntese de um novo tipo de *trans*-A_2B-corróis contendo uma porção oxima. Neste contexto, o projeto concentrou-se no desenho e síntese química de novos corróis, e na avaliação *in vitro* do seu potencial uso como PS em PDT de cancro do pulmão.

Na **Parte A** deste trabalho, três novos compostos desta nova biblioteca química de corróis foram sintetizados. Isso foi conseguido por meio de duas reações consecutivas de hetero-Diels-Alder ou adições conjugadas de nitrosoalcenos, gerados *in situ* a partir de desidrohalogenação de α,α-dihalo-oximas, com dipirrometanos, seguida de macrociclização oxidativa com 2,3-dicloro-5,6-diciano-1,4-benzoquinona (DDQ). Os PS foram caracterizados por ^{1}H RMN, ^{13}C RMN, ^{19}F RMN e espectrometria de massa. De seguida, foi realizada sua caracterização fotofísica em conjunto com corroles previamente sintetizados no Grupo de Química Orgânica.

Na **Parte B**, estudos *in vitro* desses corróis baseados em PDT foram realizados em linhas de células de cancro do pulmão. Para isso, os PS foram solubilizados em dimetilsulfóxido (DMSO) e administrados às linhas celulares A549 e H1299 em diferentes concentrações que variaram de 50 nM a 10 µM. Em seguida, as células foram incubadas por 24 horas, e duas experiências diferentes foram realizadas, de forma a avaliar a fotocitotoxicidade e a citotoxicidade. Para os ensaios de fotocitotoxicidade, as culturas foram lavadas com PBS, irradiadas com um fluxo de fotões de 7,5 mW/cm^2, até um total de 10 J, e incubadas por 24 horas antes dos ensaios de MTT e SRB. Para os ensaios de citotoxicidade, as culturas foram lavadas com PBS e incubadas por 24 horas antes dos ensaios MTT e SRB.

Os ensaios preliminares de MTT de alguns desses PS mostraram que, quando sob irradiação, o valor da concentração para 50% de inibição da atividade metabólica (IC_{50}) estava na faixa dos nanomolar: 270 nM em H1299 e 127 nM em A549. Os ensaios SRB corroboram os resultados descritos anteriormente. Na verdade, os valores de IC_{50} foram semelhantes aos de outros medicamentos de PDT clinicamente aprovados, como Foscan®. Além disso, todos os corróis mostraram ausência de citotoxicidade no escuro em ambas as linhas celulares.

A alta fotocitotoxicidade e a ausência de citotoxicidade dos *trans*-A_2B-corróis corrobora sua aplicabilidade como PS em PDT, apontando para um efeito terapêutico promissor, e suporta estudos futuros.

Palavras-chave:

Terapia fotodinâmica, corróis, *trans*-A_2B-corróis, cancro do pulmão, fotocitotoxicidade.

Table of contents

Abbreviations

AD	adenocarcinoma
b	optical path travelled by light
br s	broad singlet
c	concentration
d	doublet
DC	dendritic cells
DDQ	2,3-dichloro-5,6-dicyano-*p*-benzoquinone
DMEM	Dulbecco's Modified Eagle's Medium
DMSO	dimethyl sulfoxide
DMSO-d_6	hexadeuterodimethyl sulfoxide
DNA	deoxyribonucleic acid
DP	dipyrromethane
ER	endoplasmic reticulum
ESI	electrospray ionization
HOMO	highest occupied molecular orbital
HRMS	high resolution mass spectrometry
Hz	hertz
IC	internal conversion
IC_{50}	concentration value for the 50% inhibition of the metabolic activity
IL-1β	interleukin-1β
IL-6	interleukin-6
IR	infrared
ISC	intersystem conversion
J	coupling constant
LCC	large cell carcinoma
LDL	low density lipoprotein
LUMO	lowest unoccupied molecular orbital
m	multiplet
mAb	monoclonal antibody
Me	methyl
*m*THPC	5,10,15,20-tetra(*m*-hydroxyphenyl)chlorin
MTT	3-(4,5-dimethylthiazol-2-yl)-2,5-diphenyltetrazolium bromide
MW	multiwell plate
NIR	near-infrared
NMR	nuclear magnetic resonance
NP	nanoparticle

NSCLC	non-small cell lung carcinoma
PBS	phosphate buffer saline
PDT	photodynamic therapy
Ph	phenyl
ppm	parts per million
PS	photosensitizer
R^2	coefficient of determination
ROS	reactive oxygen species
r.t.	room temperature
s	singlet
S_0	ground state
S_1	singlet excited state
S_n	singlet excitation states
SCC	squamous cell carcinoma
SCLC	small-cell lung carcinoma
SRB	sulforhodamine B
T_1	triplet excited state
TFA	tetrahydrofuran
THF	tetrahydrofuran
THF-d_8	octadeuterotetrahydrofuran
TLC	thin layer chromatography
TNF-α	tumor necrosis factor α
TPP	tetraphenylporphyrin
WHO	World Health Organization
ε	molar absorptivity coefficient
Φ	quantum yield
Φ_Δ	singlet oxygen quantum yield
Δ	chemical shift
λ	wavelength

Chapter 1: Introduction

Over the last decades, questions such as “what causes cancer” or “will we ever find the cure for cancer” have intrigued humanity.

Cancer develops when cells grow, divide, and re-divide out of control, instead of being replaced by new cells able to comply with normal homeostasis.[1] This abnormal behavior generally results in a progression from a pre-cancerous lesion to a malignant tumor.

Despite the complex causes, the roots of the aforementioned alterations are mainly the acquired mutations caused by interactions between a person's genetic factors and three categories of external carcinogens: physical carcinogens, such as ultraviolet or ionizing radiation; biological carcinogens, such as infections from certain viruses, bacteria, or parasites; and chemical carcinogens, such as components of tobacco smoke or other poluents.[2] It is also relevant to note that as a person gets older, the tendency is for cellular repair mechanisms to become less efficient, making ageing another risk factor for cancer.[3] Germline mutations might also be in the origin of cancer, but in less significant numbers.[4,5]

It is also important to point out that the economic impact of cancer is significant and is increasing on a yearly basis. The total annual economic cost of cancer was estimated at approximately 1.16 trillion (10^{12}) dollars.[6] Cancer numbers are growing worldwide, driven by demographic growth, ageing and socioeconomic development.[7] As result, cancer is expected to rank as the leading cause of premature death (death below the age of 70 years) in the 21st century,[7] being projected to increase from 14 million annual cases documented in 2012 to 22 million within the next two decades.[6,8] It is in Europe that these numbers are more alarming. According to estimates from the World Health Organization (WHO), cancer is now the leading cause of premature death in 28 of the 40 European countries and is the second most common in the remaining countries.[5]

Globally, lung and breast cancers are the most common forms of cancer, with 11.6% of the total cases each in 2018.[7] Lung cancer is also the leading cause of cancer related death (18.4% of the total cancer deaths), with a focus on developed countries, as shown in Figure 1.[9]

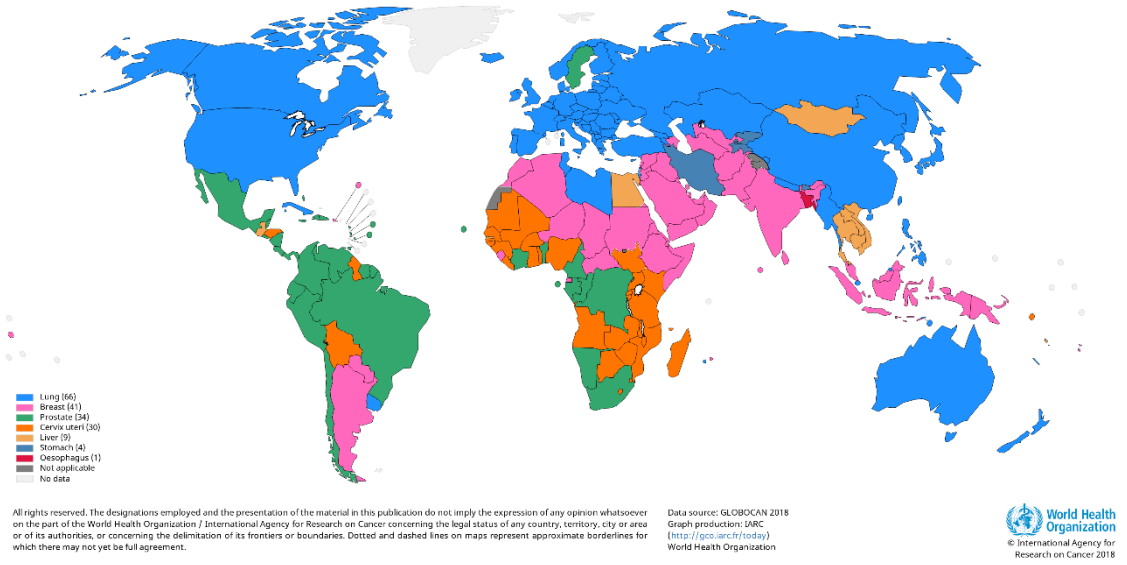

Figure 1: Top cancer per country, estimated age-standardized mortality rates (World) in 2018, both sexes, all ages. Based on World Health Organization.[10]

Lung cancer

About 90% of lung cancers are related to smoking and the use of tobacco products[11]. Histologically, lung cancer is divided into two broad classes: small-cell lung carcinomas (SCLC) and non-small cell lung carcinomas (NSCLC).[12] SCLCs are highly malignant tumors and account for 15% of all lung cancers. NSCLC, which account for the remaining 85%, are further subdivided into few subtypes: adenocarcinoma (AD, 40% of all lung cancers), squamous cell carcinoma (SCC, 25-30% of all lung cancers) and large cell carcinoma (LCC, 5-10% of all lung cancers).[12–16]

Table 1: Lung cancer types.[17]

Lung Cancer Type		**% of Lung Cancer**		**Anatomic Location**
NSCLC	AD	85%	40%	Arise in peripheral bronchioles (more peripheral)
	SCC		25-30%	Arise in main bronchi and advance to the carina (more central)
	LCC		10%	Tumors lack the classic glandular or squamous morphology (more peripheral)
SCLC		15%		Derive from the hormonal cells and disseminate into submucosal lymphatic vessels and regional lymph nodes almost without a bronchial invasion (more central)

Note: NSCLC, non-small cell lung carcinoma; AD, adenocarcinoma; SCC, squamous cell carcinoma; LCC, large cell carcinoma; SCLC, small-cell lung carcinoma.

Cancer Treatment

From the first reports in which cancer was described for centuries as an incurable disease,[18] through the introduction of cisplatin in the 20th century,[8] to the present day where medical advances have allowed the development of personalized therapies, the prognosis of a cancer patient improved exponentially. Today, cancer treatment consists of a multifactorial approach, in which various therapies, such as surgical, chemo, radio, immune and hormonal, are combined according to the diagnosis and stage of cancer.[19,20]
The mainstay for lung cancer treatment includes surgery, chemotherapy, radiotherapy and targeted therapies.[11] Although early stages of this type of cancer can be effectively treated by surgery and adjuvant chemotherapy, advanced stages are unresectable.[21] Furthermore, the form of treatment for early stages is invasive and associated with long periods of recovery.[1,22] Neo-adjuvant or adjuvant chemotherapy with cytotoxic agents that are not specifically targeted at tumor cells has been also a standard approach. As this cytotoxic drugs are systemically administered, chemotherapy have adverse effects on healthy tissues, besides killing cancer cells.[22] Radiotherapy, a directed form of cancer treatment, uses a high-energy X-ray beam or hadrons to destroy cancer cells and slow tumor growth with few harming effects on nearby healthy tissues.[23] However, patients tend to experience uncomfortable side effects such as burned skin in the projected tumor region, fatigue, sore throat and cough, and difficulty in breathing due to limitation of lung capacity, as a consequence of radiation effects.[1,22]
The photodynamic therapy (PDT) proposes to be not only an adjuvant therapy that allows to significantly improve the prognosis and quality of life of patients without significant side effects, but also a neoadjuvant therapy in cases of not operable patients or unresectable tumors.[24–26]

Photodynamic therapy

PDT is used in certain neoplastic and non-neoplastic diseases, combining three elements that are non-toxic individually: a photosensitizer, visible light of a specific wavelength, and molecular oxygen.[27–30] Over the last decades, this therapy has been the focus of intense research, because it allows localized application, it is little invasive, and has few side effects.[31,32]
PDT can be curative, particularly in early stage tumors. It can prolong survival in patients with unresectable cancers and significantly improve quality of life. These properties make it a valuable therapeutic option *per se* or for combination with other treatments.[28,33,34]

In oncology, several PDT protocols are approved, including for cancers of digestive tract,[35–38] head and neck,[39] lung and malignant pleural mesothelioma,[40] cervix, bladder, non-melanoma skin cancer, and basocellular carcinoma.[41]

PDT fundamentals

PDT is mediated by a photosensitizer, a non-toxic molecule,[33] which is able to initiate a photochemical and photophysical process, after being irradiated by tissue-penetrating wavelengths of visible light or near-infrared (NIR) spectral region.[28] Figure 2 shows the absorbance of hemoglobin and water as a way to evidence the phototherapeutic window, which is the absorbance band ideal for photosensitizer activation.

The generation of highly reactive products termed reactive oxygen species (ROS)[42] occurs as a product of the photodynamic reaction. Within ROS, singlet oxygen ($^1O_2$) is particularly relevant, being a very reactive species despite having a short lifetime inside cells, up to 300 nanoseconds.[27,43] This circumstance limits its diffusion and maximum range of reactive action to only approximately 20 nm,[28,44–46] therefore very localized cytotoxicity toward malignant cells is elicited, leading to cell death via apoptosis or necrosis.[27,28]

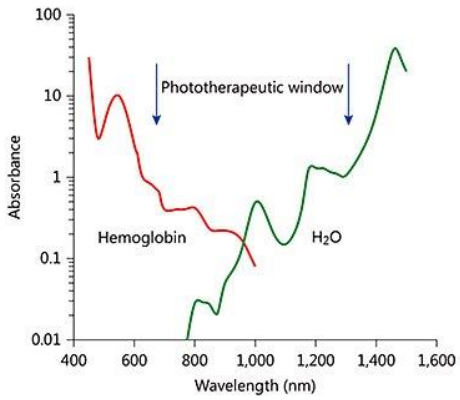

Figure 2: Therapeutic window, where the absorption and scattering of light by tissues is minimal. For simplicity, absorption by hemoglobin and water is presented in the logarithmic scale.[54]

From these particularities on which PDT is dependent results a double selectivity. This selectivity is based upon the preferential absorption and retention of the photosensitizer by tumor cells and on the localized irradiation of the cancer region.[22] Selective photosensitizer absorption and retention by tumor cells depends on chemical properties of the molecules, but is often associated with the specific microenvironment of most solid tumors, once they have fenestrated blood capillaries, reduced lymphatic drainage and low pH.[47,48]

The clinical procedure, schematized in Figure 3, involves systemic or topic administration of a photosensitizer that accumulates into tumor cells, followed by its irradiation and activation with a light source of a wavelength corresponding to the absorbance band of the photosensitizer. A series of events lead to direct tumor cell death, damage of the microvasculature associated with tumor, which contributes greatly to tumor destruction,[22,41] and induction of an inflammatory reaction that can lead to the development of systemic immunity for effective destruction of metastases.[28,31]

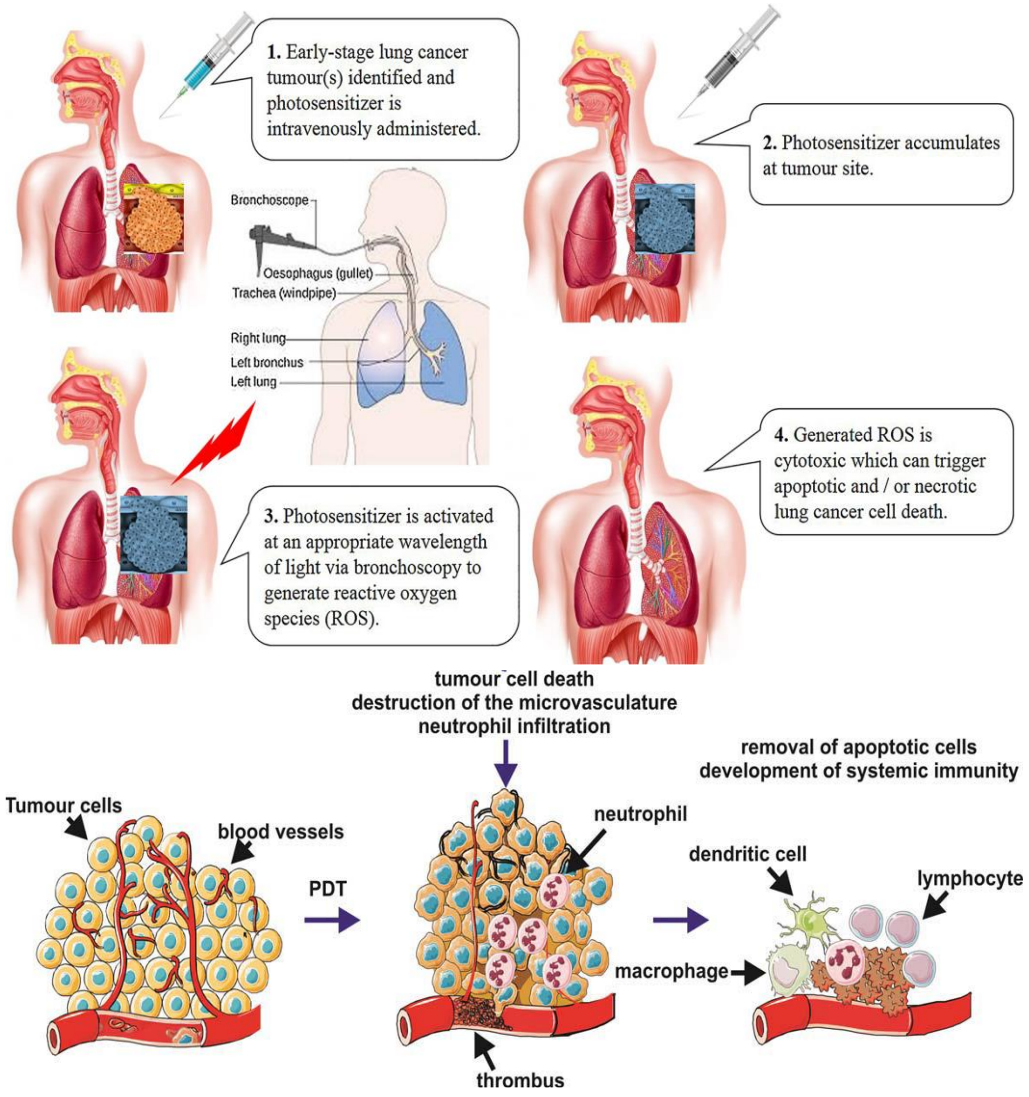

Figure 3: Principles of photodynamic therapy (PDT). 1. Photosensitizer (PS) drug is administered to the patient 2. The PS then accumulates at the tumor site 3. Once the PS is absorbed by the tumor, irradiation at an appropriate wavelength (600 nm–800 nm) is then applied to activate the PS 4. This activation leads to the selective destruction of tumor cells via apoptotic, necrotic, or autophagic mechanisms, accompanied by induction of an acute local inflammatory reaction that participates in the removal of dead cells, restoration of normal tissue homeostasis, and, sometimes, in the development of systemic immunity.[22,28]

PDT advantages and disadvantages

PDT treatment for lung cancer has several advantages.[24] It is cost effective, simple, easily controllable,[27] minimally invasive, can be repeated and has little or no scar after healing.[22,41]

The mechanism of action of photodynamic therapy also gives it some advantages. PDT is a local therapy[49], having no long-term side effects.[50] As none of the clinically approved PSs accumulate in cell nuclei, DNA damage that could be carcinogenic or lead to the development of resistant clones is limited.[28] Moreover, mutations that confer resistance to radiotherapy or chemotherapy do not compromise the antitumor efficacy of PDT.[28]

Among limitations, temporary cutaneous and ocular photosensitivity reactions have been identified as the most significant disadvantages. This occurs due to photosensitizer accumulation in these organs, forcing patients to avoid sunlight until photosensitizer levels decrease to safe values.[51] As such, it is essential that new photosensitizers have fast kinetics and rapid elimination from the organism.[51] Furthermore, deep located tumors are hard to treat due to low tissue penetration of visible light.[22]

The previously referred advantages and disadvantages are summarized in Table 2.

Table 2. Advantages and disadvantages of Photodynamic Therapy.

PDT for cancer	
Advantages	**Disadvantages**
-Fewer adverse effects -Little invasiveness -Short treatment time -Usable in outpatient settings -Double selectivity -No resistance mechanisms -Can be applied at the same location several times -Little or no scar after healing -Lower costs than other treatments -Protect the appearance of organs	-Photosensitizer water insolubility -Photosensitivity after treatment -Deep located tumors are hard to treat

PDT photochemistry and photophysics

Photophysics and photochemistry are important concepts regarding PDT. They are concerned with describing the physical and chemical processes induced by the light absorption, involving energetic, structural, and dynamic studies. A molecule, when absorbing light and being excited, can lose its energy through physical processes or participate in chemical reactions. To quantify each of these processes, quantum yield (Φ) measurements are used. In PDT the singlet oxygen quantum yield (Φ_Δ) is a relevant measurement of the efficiency in which photosensitizers are able to use energy from light to convert oxygen in the ground state to the reactive species singlet oxygen ($^1O_2$).[52] In imaging for cancer diagnosis, fluorescent quantum yield is another relevant quantitative measurement, and is the ratio of the number of photons emitted by the number of photons absorbed.[53]

All particles, when not excited, tend to stay in their ground state (S_0), i.e. the least possible energy in a physical system. In a photosensitizer, this usually means that it has 2 electrons with opposite spins located in a most energetically favorable molecular orbital.

However, the incidence of a photon on a photosensitizer in its ground state (S_0) can provide sufficient energy to transfer one of the electrons from the highest occupied molecular orbital (HOMO) to the lowest unoccupied molecular orbital (LUMO) or to a higher energy orbital. This means that the photosensitizer either is excited to its first singlet excited state (S_1) or to a multitude of higher energy singlet excitation states (S_n), respectively. The different singlet excitation states (S_n) have crescent energies, but they all tend to decay to the first singlet excited state (S_1) by internal conversion (IC). Once in this excited stage, the PS can experience two types of processes: one radiative and one non-radiative.[28,54]

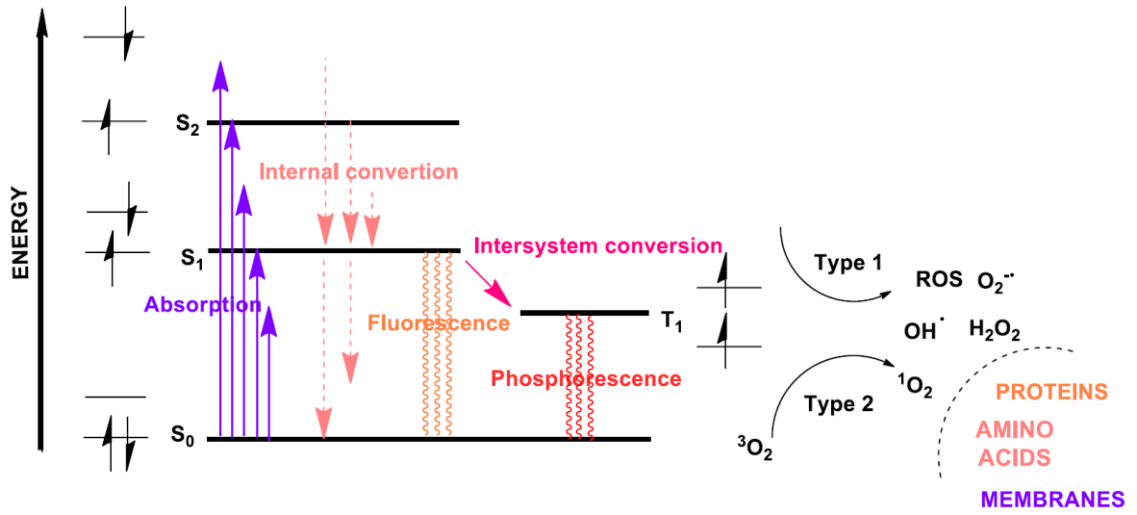

Figure 4: Perrin-Jablonski energy diagram for a photosensitizer (PS). After excitation to the singlet excited state the PS may either decay back to the ground state (by fluorescence emission or non-radiative decay) or undergo intersystem conversion (ISC) to the triplet excited state (T_1). From the triplet state, the PS may undergo excited state reactions to generate reactive oxygen species (ROS), cytotoxic to the cell.

In the radiative process, the PS returns to the S_0 and emits a photon in a process called fluorescence. When the photon is emitted, it has less energy than the absorbed photon. This energy difference is the Stokes shift.[2,47,48,55–57] Although this process does not initiate the photodynamic reaction with therapeutic effect, this property can potentially be used for diagnosis by obtaining fluorescence images.[2,58,59]

Alternatively, in the non-radiative process, one electron undergoes a spin inversion, called intersystem crossing (ISC), to form a more stable triplet excited state (T_1) (Figure 4).[54,60] The photosensitizer in T_1 can either decay radiatively to the S_0 in a process called phosphorescence (Figure 4) or undergo quenching (nonradiative de-excitation process). The latter is the decisive mechanism of the photodynamic reaction, triggering two types of reactions, Type I and Type II (Figure 4). Both reactions occur simultaneously, and the ratio between them depends on the type of photosensitizer used, the substrate and oxygen concentrations and the amount of available oxygen.

In the Type I reaction, the photosensitizer in the T_1 state reacts directly with biomolecules in the cellular microenvironment, with the transfer of an electron or a proton between them, to form a pair of radical anion ($PS^{-}\cdot$) and radical cations (biomolecule$^{+}\cdot$).[45,61,62] This photosensitizer radical anion is likely to instantly react with molecular oxygen ($^3O_2$), donating its extra electron to produce the superoxide anion (O_2^{-}) and restoring the PS. In biological systems, this radical reacts with water to produce hydrogen peroxide (H_2O_2) that can cross cell membranes and cause damage directly on cell compartments. At higher concentrations, the superoxide anion can form powerful and virtually

indiscriminate oxidant hydroxyl radicals (HO•). Besides being the most reactive ROS, HO• has the shortest lifetime and diffusion distance[63], which confines biomolecules oxidation to a small range within the cell.[2,64]

In the Type II reaction, the T_1 state of the PS transfers its energy directly to ground state oxygen ($^3O_2$). This energy not only promotes one of its parallel spinning electrons to a high-energy orbital but also inverts its spin, producing the excited state of oxygen - the singlet oxygen ($^1O_2$) (Figure 5).[54] This change removes the spin restriction typical for triplet oxygen, and makes singlet oxygen highly reactive.[54] Its lifetime, and consequently its diffusion distance, are very limited by both physical and chemical quenching. This characteristics mean that singlet oxygen can only interact with and oxidize biomolecules and structures within its short range of action.[54] The efficiency of the Type II reaction depends on the duration (lifetime) of the triplet state and the triplet quantum yield of the photosensitizer.

In PDT, the singlet oxygen formed in Type II reaction is considered the main cytotoxic species formed during the photodynamic process.[65,66]

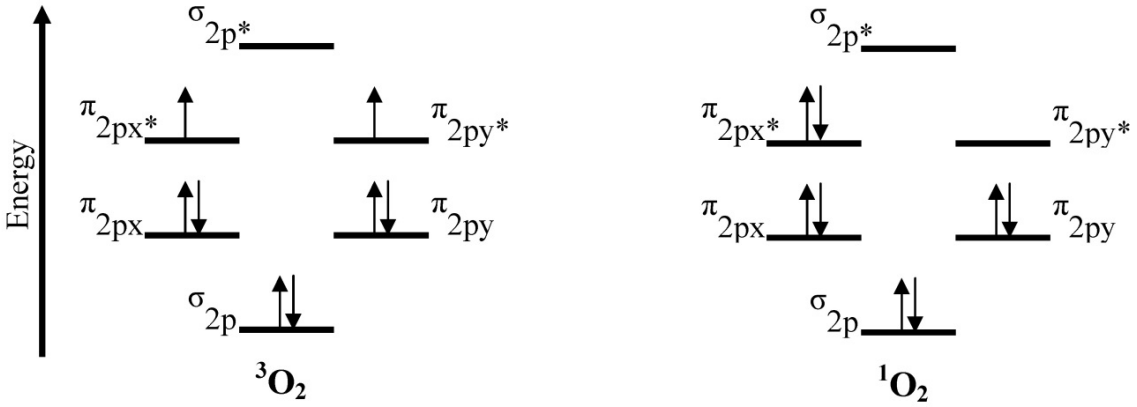

Figure 5: Electronic configuration of triplet ($^3O_2$) and singlet ($^1O_2$) states of oxygen.[67]

Reactive oxygen species (ROS) are known to trigger various reactions with biomolecules in biosystems.[68] Usually, targets are electron-rich compounds such as amino acid residues in proteins, unsaturated lipids such as cholesterol, and bases of nucleic acids. Oxidation of these targets may lead to potential destruction of cell membranes and deactivation of enzymes. These interactions activate the expression of transcription factors and cytokines, and release a number of mediators responsible for the process of cell death.[69]

Mechanisms of tumor cytotoxicity

PDT acts through three main mechanisms of tumor destruction: directly kills tumor cells, disrupts the tumor vasculature, thereby compromising the supply of oxygen and essential nutrients, and triggers an inflammatory and immune response.[70]

As mentioned earlier, ROS mediated cell death can occur by apoptosis and/or necrosis. However, autophagy can also take place, and under *in vivo* conditions, ROS-mediated tumor vascular shut down and activation of immune response through the induction of inflammatory reaction also play a crucial role in the therapeutic outcome of PDT.[69]

ROS triggers a cascade of molecular events that contribute to direct tumor cell death. The three main mechanisms of cell death - necrosis, apoptosis and cell death associated with autophagy - may occur simultaneously in the same cell population. Recent studies point out that apoptosis is probably the main mechanism, but this may be influenced by factors such as the cellular organelles where the PS molecules is located at the time of irradiation.[71] Typically, photosensitizers located in the mitochondria or endoplasmic reticulum (ER) induce cell death by apoptosis,[72] whereas PS located on the plasma membrane or lysosomes may induce cell death by necrosis. Autophagy is activated in an attempt by the cell to repair itself and survive damage caused to certain key organelles. However, if this response fails, it can lead to cell death signals.[71,73]

The intensity of PDT protocols also influences the outcome. The more intense protocols (high doses of PS, high light doses, and/or short times between PS administration and irradiation) tend to cause extensive necrotic cell death, while less intense protocols favor cell death by apoptosis.[2,74]

Antivascular effects of PDT

The growth of solid tumors depends on their capacity of angiogenesis, that is, to induce the growth of blood vessels and to supply with nutrients and oxygen.[46] Besides direct cytotoxic effects on cancer cells, PDT can also trigger another 2 intra-related mechanisms: damage to the tumor vasculature, and induction of an inflammatory response.[28]

While direct cell cytotoxicity is triggered by the irradiation of photosensitizers internalized by tumor cells, the damage in the tumor vasculature is caused mainly when the irradiated photosensitizer is confined in the bloodstream, accumulated in the endothelial cells, or still attached to vessel walls, inducing loss of the tight junctions in the endothelial cells.

The consequent morphological changes within the vessel lumen lead to thrombus formation in tumor blood vessels, and induce a cascade of reactions, namely, platelet aggregation, release of vasoconstricting molecules, lymphocyte adhesion, and

increased vascular permeabilization.[48,58] This collapse of the microvasculature associated with intra-tumor microhaemorrhage can cause severe hypoxia and ischaemia.[47,48,50,75,76] Therefore, there has been a great deal of research into the development of a PDT regimens both targeted for tumor cells and for tumor vasculature itself.[2,50,58]

Inflammatory and immune response to PDT

A hallmark of PDT is the induction of acute inflammatory reaction,[46,77] which can lead to the enhancement of the immune response and to the development of immunity, with potential impact in the long term tumor control and of metastases.[28] However, PDT can also trigger immunosuppressive response in certain circunstances.[78,79]

The acute inflammatory reaction is triggered by the primary effects of PDT, such as direct destruction of tumor cells by necrosis, vessel occlusion and ischemia. This lead to the secretion of pro-inflammatory cytokines (innate immunity), for instance tumor necrosis factor α (TNF-α), interleukin-1β (IL-1β) or interleukin-6 (IL-6), thereby activating adaptive immunity components - neutrophils, mast cells, macrophages and dendritic cells - which converge on the treated site and restore homeostasis.[74,77,80,81] Crosstalk between innate immunity and adaptive immunity is established through dendritic cells (DC). In PDT, the release of inflammatory mediators in the treated area activates DCs. When activated, these cells have the capacity to pick up tumor antigens, migrate to the nearest lymph nodes, and present the antigens to $CD4^+$ T lymphocytes, making them active. In turn, these cells activate $CD8^+$ effector and memory T lymphocytes, which recognize and destroy tumor cells.[28,47,74,82] These cells are important to long term tumor control, allowing the eradication of metastases that are far from the irradiated site.[83] These characteristics suggest that, in addition to the role of PDT as a therapeutic modality, PDT-generated vaccines may have clinical potential as an adjuvant therapy.[84]

Photosensitizers

An ideal PS must possess the following characteristics: chemical purity, chemical and physical stability, rapid clearance from the body, strong absorption in the red/infrared wavelength region (600-800 nm) allowing for optimal tissue penetration, selective affinity for tumor cells, and low quantum fluorescent yield. Furthermore, it must also have a triplet state with a high half-life, a partition coefficient suitable for the intended route of administration and must allow dissolution in biocompatible formulations, if necessary.[22,67,85–88]

The photosensitizers are classified into three groups according to their functional capabilities into first, second and third generation.[86] The first clinical approved PDT drug was Photofrin®, followed by Foscan® a few years later. These are both porphyrin derivatives and respectively from first and second generation.[89] Second generation molecules are more tumor-selective, and have increased depth tissue penetration of light with a longer wavelength (650 nm–800 nm).[22] The third PSs generation consists of molecules which have been bound to moieties such as monosaccharides, peptides, low density lipoproteins (LDLs), polymers, nanoparticles (NPs) or monoclonal antibodies (mAbs), in order to increase selectivity or provide targeting.[90]

Over the last decades, there has been a great deal of work on new molecules, most of them based on macrocycles of the porphyrins family, and some derivatives have reached advanced stages of clinical testing.[91] In fact, porphyrins, phthalocyanines, chlorins and corroles (Figure 6) create a compact group of macrocyclic compounds of established utility in medicine and technology, particularly in PDT.[92,93]

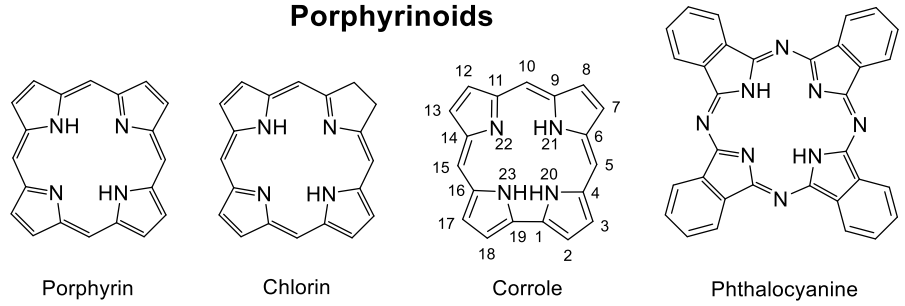

Figure 6: Examples of porphyrinoids, a class of functional molecules of tetrapyrroles that differ in the level of oxidation and in the macrocycle structure: porphyrin, chlorin and phthalocyanine structure, and corrole structure and numbering.[92]

Corroles

Corroles are a ring-contracted tetrapyrrolic macrocycles of the porphyrin family, containing three methine bridges and a direct pyrrole-pyrrole linkage.[94] They were first introduced in 1960s, partly due to the interest in vitamin B_{12}. In 1999, with the development of the first direct synthesis of corroles from pyrrole,[95] this analogue of porphyrin started receiving more attention. Corroles derivatives have demonstrated extensive usage not only in the field of antitumor drugs development as photosensitizers (PS) in photodynamic therapy (PDT), but also in catalytic oxidation, synthetic organic reactions, chemical sensors, and dye sensitized solar cells.[89,96]

Meso-substituted corroles are a group of corroles with substituent groups attached to carbon 5, 10 and 15 that has been widely explored. In Figure 7 it is schematized the differences between the four types of meso-substituted corroles.

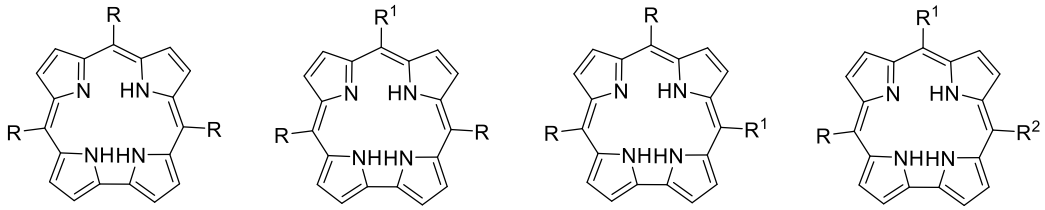

Figure 7: Meso-substituted corroles: A_3-corroles (A = R), *trans*-A_2B-corroles (where A = R and B = R^1), *cis*-A_2B-corroles (where A = R and B = R^1), and ABC-corroles (where A = R, B = R^1, and C = R^2).

After PDT, morphological changes observed with the different corroles point to tumor cells usually turning rounding and blebbing after treatment, typifying the cell death via the apoptosis pathway. Necrosis characteristic morphology has been observed only in few cases so far.[89]

Figure 8.A shows the molecular structures of the tetraphenylporphyrin (TPP) and the halogenated corroles which were explored by Liu.[97] When compared to porphyrin, corroles are macrocyclic aromatic compounds, which lack one *meso* carbon. This small difference is sufficient to give it some advantages over the other porphyrinoids, such as stronger Q band absorption of long visible wavelengths (Figure 8.B),[97] stronger fluorescence, and especially easier metabolism characteristics due to their less structural robustness.[89] The absorption spectra represented in Figure 8.B shows a strong Soret band (or B band) around 420 nm, and several weak Q bands between 450 and 650 nm, exhibiting much stronger Q band absorption than that of porphyrin. It is also possible to see a red shift of the Q bands of the corroles compared to porphyrin, which indicate that corroles are more suitable as a PDT photosensitizer than porphyrin compounds.

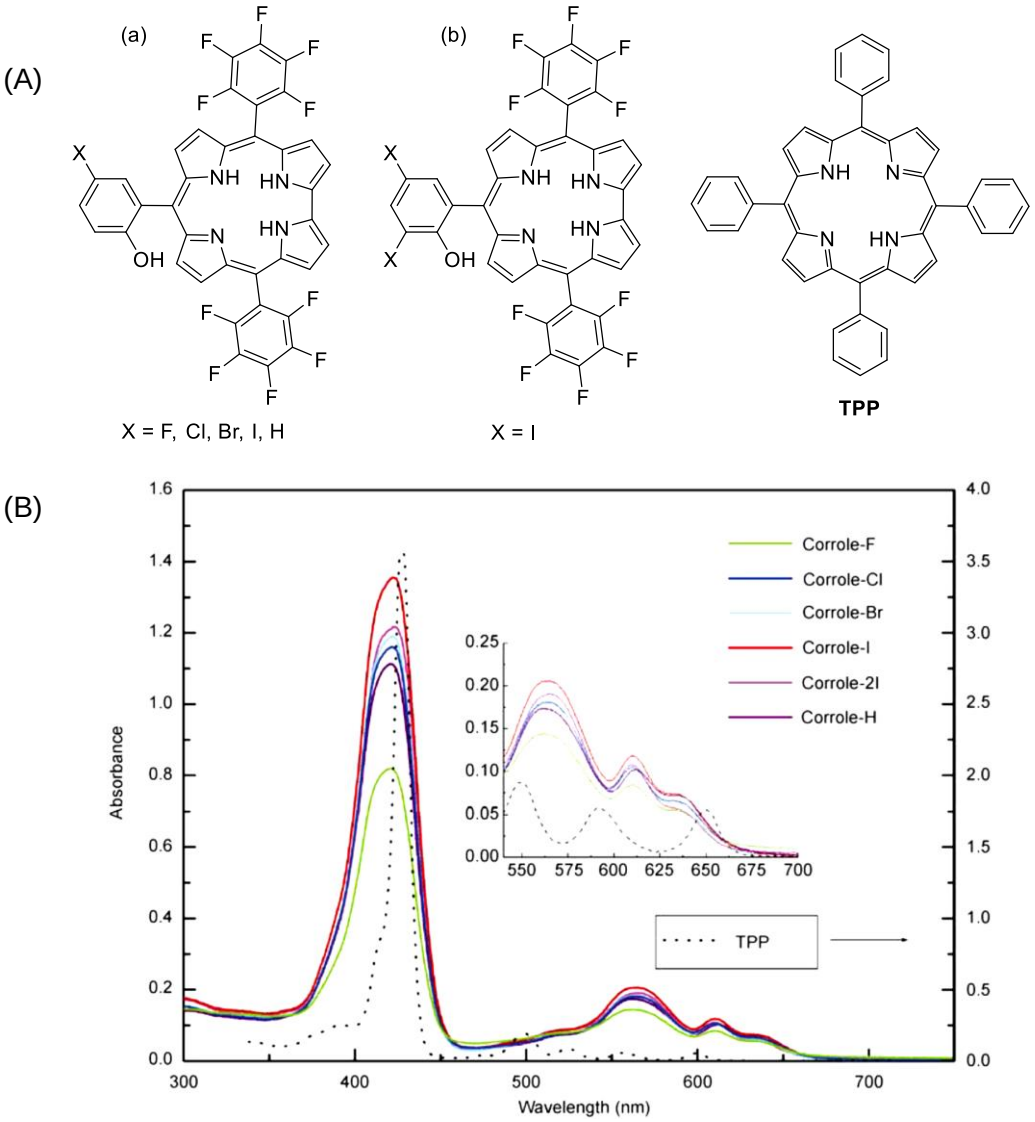

Figure 8: (A) Structures of halogenated corroles mono-hydroxyl (a) and double-hydroxyl (b), and TPP. (B) UV-Vis absorption of corrole halogen derivatives and TPP in toluene. Adapted from You et al. 2010.[97]

Free-base corrole's structure and photophysical properties has been the focus of many researches aiming for stronger absorption Q bands from 600 to 800 nm. Bevilacqua and coworkers demonstrated that the absorption spectrum, specifically the Q bands, is affected by the donor or acceptor character, and the position of the substituents groups.[98] Besides Alberto et al. noticed that the presence of iodine, a heavy atom, can cause a redshift of the Q band.[99] Therefore, it is possible to adjust corroles structure, particularly on β- and *meso*- positions of the macrocycle, to increase their absorption in useful wavelengths, increasing their potential to be used *in vitro* and *in vivo*.

Numerous studies have found that changes in the structure also influence the photochemical characteristics and, ultimately, the phototoxicity of the corroles. Zhao and

coworkers showed that the increase of iodination enhanced intersystem crossing and triplet quantum yield, and decreased the singlet oxygen ($^1O_2$) quantum yield.[100] Additionally, Shao noticed triplet quantum yield increased with the increase of monohydroxyl halogen atomic weight and with the replacement of hydrogen atoms of *meso*-phenyl groups for fluorine atoms.[101] Shi et al. observed the increase of atomic height of the substituted halogen lead to the decrease of fluorescence quantum yield and increase of triplet quantum yield.[102]

The cellular uptake is another factor to consider since effective photosensitizers must have high cellular uptake.[103] Among others, this feature can be decreased by the presence of β-cyclodextrin moiety,[104] and increased with glycosylation of corroles[105] or by the presence of the thien-2-yl moiety (corrole **5**).[106] Zhang et al. verified that the addition of *meso*-ethoxycarbonyl substituents allowed for cell membrane penetration without the help of an internalizing protein.[107] These observations show that the molecular structure of the corrole greatly influences cellular uptake.

Figure 9 compiles some highly promising corroles which photocytotoxicity and dark toxicity was tested *in vitro*. Hydroxylamino corroles **1** and **2** showed photocytotoxicity toward carcinoma cell lines A549 (lung) and BEL-7402 (endocervical), quite comparable to *meso*-tetra(*p*-hydroxylphenyl)porphyrin (TOPP), suggesting that they are worthy of further testing.[108] Anionic sulfonated corrole **3** and its gallium, aluminum, and manganese complexes showed potential of proliferation inhibition against cancer cell lines MDA-MB-231 (breast), SK-MEL-28 (melanoma), and OVCAR-3 (ovarian), particularly the one with gallium in the central core.[109] Free-base corrole **3** showed high photocytotoxicity to A549 cells (IC_{50} = 5.0 μM), and *in vivo* assays revealed a significant decreased in tumor growth (A549 xenografted tumor), without obvious loss of mice body weight.[110] Interestingly, Sn(IV) corroles **4** and **5** showed photocytotoxicity and no dark cytotoxicity to MCF-7 breast cancer cells, with values of IC_{50} of 3.2 and 13.1 μM after irradiation. The difference between the IC_{50} of these two corroles was attributed to the higher singlet oxygen quantum yield and lipophilicity of corrole **5**.[106] Carboxaldehyde corroles **6** and **7** exhibited very low dark cytotoxicity but high photocytotoxicity to A549 and SiHa (cervical) cell lines.[89] Mono-hydroxyphenyl metallocorroles **8a**–**c** showed low or no dark cytotoxicity to A549, HepG2 (liver), MCF-7, DU145 (prostate) carcinoma cell lines, and to GES-1 gastric epithelial (non-malignant) cell line. **Fe-8c** corrole showed the greatest potential for PDT, with values of IC_{50} of 30 μM against A549 lung cancer cells, inducing cell apoptosis and necrosis, high cellular ROS level and disruption of the mitochondrial membrane potential.[111] The amphiphilic hydroxyl corrole **9** and its gallium complex **10** also showed very low dark cytotoxicity and high photocytotoxicity toward carcinoma cell lines A549, BEL-7402, and SiHa.[112] Phosphorus corrole **11** presented little dark toxicity,

and high photocytotoxicity against H460 and A549 lung cancer cell lines, with values of IC_{50} of 1.2 and 1.7 μM, respectively.[113] Corroles **12** and **13** bearing methyl benzoate group(s) showed high photocytotoxicity toward QGY-7701 (hepatocellular carcinoma; IC_{50} values of 3.58 and 3.92 μM, respectively) and MHCC-H/L (hepatocellular carcinoma; IC_{50} values of 9.62 and 16.02 μM, respectively) cells, and low dark toxicity toward the same cell lines.[89]

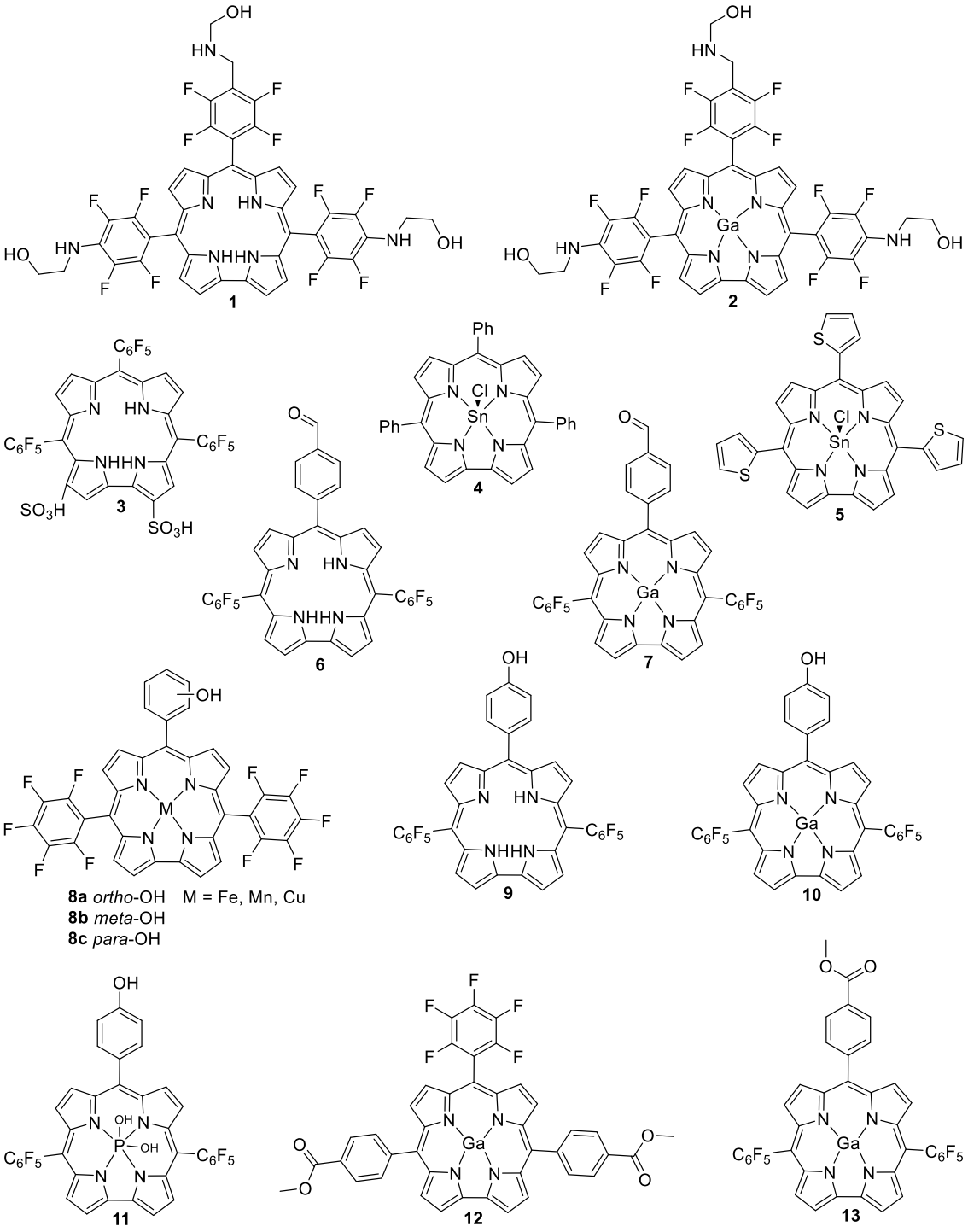

Figure 9: Examples of corroles tested in different cell lines as photosensitizers in PDT.

In short, all of these observations demonstrate that the photodynamic antitumor activity of corroles, affected by its photophysical and photochemical characteristics, and by cellular uptake, strongly depends on the molecular structure of corrole and the tumor cell lines. The relationship between corrole peripheral substitution and their antitumor activity is still a fundamental research topic in this field.[89]

Aims

PDT for the treatment of superficial non-small cell lung cancers (NSCLC) that have not spread beyond the lung itself is very promising.[114,115]

A group of corroles for which nothing is known about their possible applications is the *trans*-A_2B-corroles schematized in Figure 10. Lopes and Pinho e Melo described a novel approach to *trans*-A_2B-corroles based on the reactivity of nitrosoalkenes towards dipyrromethanes. The synthetic strategy involves the synthesis of bilanes from α,α-dihalo-oximes and dipyrromethanes followed by oxidative macrocyclization to afford a new class of tetrapyrrolic macrocycles.[116]

The aim of the project is to assess if this new class of *meso*-substituted *trans*-A_2B-corroles can offer a safe therapeutic option in PDT of lung cancer. To achieve this goal, we will focus on the design and chemical synthesis of new *trans*-A_2B-corroles containing an oxime moiety. Then, the aim is the *in vitro* evaluation of the potential use of these new compounds as photosensitizers in lung cancer cell lines.

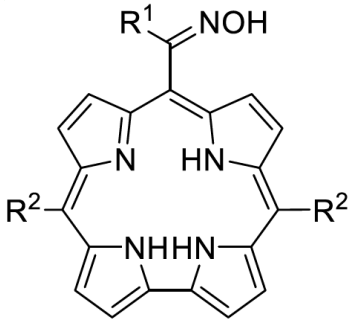

Figure 10: *Trans*-A_2B-corroles (where A = R^2 and B = $CNOHR^1$).

Chapter 2: Methods and Materials

Part A: chemical synthesis and characterization

2.A.1. Solvents and reagents

All reagents were provided by Sigma-Aldrich, Merck, Fluka or Fluorochem and used without further purification. Solvents were dried, when necessary, according to the methods described below, and distilled before use.

Dichloromethane

This solvent was refluxed in the presence of calcium chloride for 3 hours, distilled and stored on 4 Å molecular sieves.

THF

This solvent was refluxed in the presence of sodium wires, using benzophenone as an indicator, distilled, and stored on 4 Å molecular sieves.

2.A.2. Instrumentation and methodology

Thin layer chromatography (TLC)

Analytical TLCs were performed using precoated silica gel plates Macherey-Nagel Xtra SIL G/UV254 and visualized by UV irradiation (254 and 356 nm), to control the reactions and verify the purity of two compounds.

Flash chromatography

The synthesized compounds were purified by flash column chromatography using silica gel 60 (0.035–0.070 mm), provided by Acros Organics, as the stationary phase, as indicated in each case.

Nuclear Magnetic Resonance (NMR) spectroscopy

Nuclear magnetic resonance (NMR) spectra were recorded with a Bruker Avance III instrument, operating at the following frequencies: Proton (^{1}H) at 400 MHz, carbon (^{13}C) at 100 MHz, and fluor (^{19}F) at 376 MHz. Chemical shifts are expressed in parts per million

(ppm) and coupling constants (*J*) are expressed in hertz (Hz). The deuterated solvents were deuterochloroform ($CDCl_3$), hexadeuterodimethyl sulfoxide (DMSO-d_6) and octadeuterotetrahydrofuran (THF-d_8) as indicated in each case.

High Resolution Mass Spectrometry (HRMS)

High-resolution mass spectra were obtained with a TOF VG Autospect M spectrometer with electrospray ionization (ESI).

Ultraviolet-visible absorption spectroscopy

UV-Visible absorption spectra were obtained on a Shimadzu UV-2100 spectrophotometer using 1 cm optical quartz cells. The molar absorption coefficients were determined after preparation of 10 dilutions in DMSO. The maximum absorption of each band was plotted as a function of the concentration of different solutions, with the slope value corresponding to the molar absorptivity coefficient. This analogy is transmitted by the Beer-Lambert law, $A = \varepsilon bc$, where A is the absorbance, ε is the molar absorptivity coefficient, b is the optical path travelled by light and c is the concentration of the solution.

2.A.3. Synthesis of *Meso*-substituted Corroles

2.A.3.1. General procedure for synthesis of α,α-dibromoketones

α,α-Dibromoketones were prepared according to a procedure described in the literature.[117,118] A solution of bromine (10 mmol) in glacial acetic acid (2 mL) was added dropwise to a solution of the appropriate ketone (10 mmol) in glacial acetic acid (6 mL). The reaction mixture was stirred at room temperature until the bromine was completely consumed (disappearance of the red color) and the α-bromoketone precipitates. At this time, another solution of bromine (10 mmol) in glacial acetic acid (2 mL) was added dropwise. The mixture was stirred at room temperature until the bromine was completely consumed (disappearance of the red color). If the product precipitates it was filtered and washed with ethanol 50% (100 mL), if not it was purified by extraction with dichloromethane.

2,2-Dibromo-1-phenylethanone (14a)

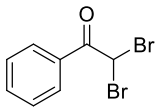

Compound **14a** was obtained from acetophenone solution (1.67 mL, 10 mmol), purified by filtration, and obtained as a white solid (2.16 g, 78% yield). The purity of compound **14a** was confirmed by TLC compared with an existing standard.

2,2-Dibromo-1-(*p*-fluorophenyl)ethanone (14b)

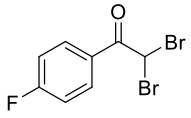

Compound **14b** was obtained from *p*-fluoroacetophenone solution (3.06 mL, 25.21 mmol) purified by extraction with dichloromethane and obtained as a white solid (5.74 g, 78% yield). ^{1}H NMR (400 MHz, $CDCl_3$): δ = 6.61 (s, 1H), 7.16-7.26 (m, 2H), 8.14-8.17 (m, 2H) ppm.

2,2-Dibromo-1-(*p*-bromophenyl)ethanone (14c)

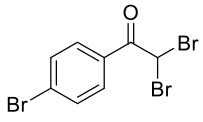

Compound **14c** was obtained from *p*-bromoacetophenone (5.00 g, 25.12 mmol), purified by filtration, and obtained as a white solid (5.88 g, 66% yield). ^{1}H NMR (400 MHz, $CDCl_3$): δ = 6.60 (s, 1H), 7.64-7.67 (m, 2H), 7.95-7.98 (m, 2H) ppm.

2.A.3.2. General procedure for synthesis of α,α-dibromo-oximes:

Oximes were prepared according to a procedure described in the literature.[119] Hydroxylamine hydrochloride (30 mmol) was added to a solution of the appropriate α,α-dibromoketone (12 mmol) in ethanol (30 mL). The reaction mixture was stirred at room temperature until the α,α-dibromoketone was completely consumed (48-72 h). After the reaction was complete (TLC control), the solvent was evaporated. The oxime was purified by addition of water and filtrated or by extraction with ethyl acetate.

(*E*) and (*Z*)-2,2-Dibromo-1-phenylethanone oximes (15a)

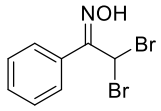

The product was obtained from ketone **14a** (2.16 g, 7.77 mmol). Extraction of the residue with ethyl acetate gave oxime **15a** as a mixture of isomers *E*/*Z* as a colorless oil (1.37 g, 60% yield). The purity of oximes **15a** was confirmed by TLC compared with an existing standard.

(*Z*)-2,2-Dibromo-1-(*p*-fluorophenyl)ethanone oxime (15b)

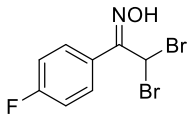

The product was obtained from ketone **14b** (5.74 g, 19.40 mmol). Extraction of the residue with ethyl acetate gave oxime **15b** as a white solid (2.19 g, 36% yield). ^{1}H NMR (400 MHz, DMSO-d_6): δ = 7.29 (m, 2H), 7.52 (s, 1H), 7.83-7.88 (m, 2H), 12.69 (s, 1H) ppm.

(*Z*)-2,2-Dibromo-1-(*p*-bromophenyl)ethanone oxime (15c)

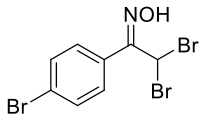

The product was obtained from ketone **14c** (5.88 g, 16.48 mmol). The addition of water to the residue and filtration gave the oxime **15c** as a white solid (3.11 g, 51% yield). ^{1}H NMR (400 MHz, DMSO-d_6): δ = 7.51 (s, 1H), 7.68-7.71 (m, 2H), 7.74-7.77 (m, 2H), 12.80 (s, 1H) ppm.

2.A.3.3. Synthesis of 5-phenyldipyrromethane (16)

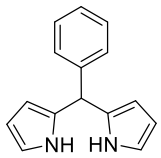

5-Phenyldipyrromethane (**16**) was prepared according to a procedure described in the literature[120]. A mixture of benzaldehyde (5.09 mL, 0.05 mol) and pyrrole (138.76 mL, 2 mol) was bubbled with nitrogen (N_2) for 10 minutes. After this time, trifluoroacetic acid (0.005 mol) was added and the mixture was stirred for 15 minutes at room temperature under N_2 atmosphere. Triethylamine was added and the pyrrole was distilled off. The crude product was purified by flash chromatography with ethyl acetate/hexane (1:6) and crystallization with cyclohexane. Dipyrromethane **16** was obtained as white solid (5.914 g, 53% yield). ^{1}H NMR (400 MHz, $CDCl_3$): δ = 5.47 (s, 1H), 5.92 (s, 2H) 6.16 (d, J = 2.8 Hz, 2H), 6.69 (d, J = 1.2 Hz, 2H), 7.17-7.33 (m, 5H), 7.90 (s, 2H) ppm.

2.1.3.4. General procedure for synthesis of bilanes

Method A: In the solvent system H_2O/CH_2Cl_2

The dipyrromethane **16** (4 mmol) and a solution of the appropriate oxime (1 mmol) in dichloromethane (2.4 mL) were added to a solution of sodium carbonate (10 mmol) in water (14.6 mL). The mixture was stirred at room temperature for 20 minutes. After this time, the reaction mixture was extracted with ethyl acetate (3 x 20 mL) and dried over Na_2SO_4, and the solvent evaporated off. The products were purified by flash chromatography.

Method B: In dichloromethane

Sodium carbonate (10 mmol) was added to a solution of dipyrromethane **16** (4 mmol) and the appropriate oxime (1 mmol) in dichloromethane (30 mL). The mixture was stirred at room temperature overnight. The reaction was monitored by TLC. Upon completion, the reaction mixture was filtered through a celite pad, and washed with dichloromethane and ethyl acetate. The products were purified by flash chromatography.

(*E*)- and (*Z*)-5,15-Diphenyl-10-[1-hydroxyimino-1-(phenyl)methyl]bilanes (17a)

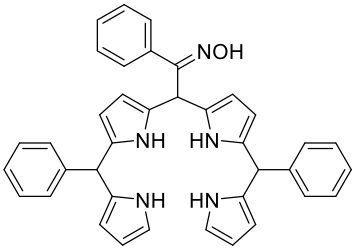

Compounds **17a** were obtained from oxime **15a** (1 mmol, 0.293 g) and dipyrromethane **16** (4 mmol, 0.889 g). Purification of the crude product by flash chromatography [ethyl acetate/hexane (1:2)] gave bilanes **17a** [Method A: 0.145 g, 25%, as a mixture of isomers *E*/*Z* (40:60); Method B: 0.189 g, 33%, as a mixture of isomers *E*/*Z* (58:42)] as a beige solid. HRMS (ESI-TOF) m/z: [M + H^+] calcd for $C_{38}H_{33}N_5O$, 576.2758; found, 576.2764.

(*Z*) isomer: ^{1}H NMR (400 MHz, DMSO-d_6): δ = 5.13 (s, 1H), 5.30 (m, 2H), 5.45−5.54 (m, 4H), 5.64 (br s, 2H), 5.85−5.89 (m, 2H), 6.58-6.59 (m, 2H), 7.04−7.06 (d, 2H), 7.09−7.32 (m, 13H), 10.39 (br s, 2H), 10.47-10.53 (m, 2H), 10.62 (s, 1H) ppm.

(*E*) isomer: ^{1}H NMR (400 MHz, DMSO-d_6): δ = 5.30 (m, 2H), 5.45−5.54 (m, 4H), 5.64 (br s, 2H), 5.85−5.89 (m, 2H), 6.58-6.59 (m, 2H), 6.14 (s, 1H), 7.04−7.06 (d, 2H), 7.09−7.32 (m, 13H), 10.39 (br s, 2H), 10.47-10.53 (m, 2H), 11.32 (br s, 1H) ppm.

(*E*)- and (*Z*)-5,15-Diphenyl-10-[1-hydroxyimino-1-(*p*-fluorophenyl)methyl]bilanes (17b)

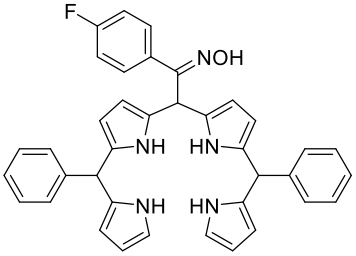

Compounds **17b** were obtained from oxime **15b** (1 mmol, 0.311 g) and dipyrromethane **16** (4 mmol, 0.889 g). Purification of the crude product by flash chromatography [ethyl acetate/hexane (1:2)] gave bilanes **17b** [Method A: 0.189 g, 32%, as a mixture of isomers *E*/*Z* (33:67); Method B: 0.190 g, 32%, as a mixture of isomers *E*/*Z* (51:49)] as a beige solid. HRMS (ESI-TOF) m/z: [M + H^+] calcd for $C_{38}H_{32}FN_5O$, 594.2664; found, 594.2661.

(*Z*) isomer: ^{1}H NMR (400 MHz, DMSO-d_6): δ = 5.13 (s, 1H), 5.28-5.31 (m, 2H), 5.46−5.56 (m, 4H), 5.63 (d, *J* = 16.4 Hz, 2H), 5.85−5.90 (m, 2H), 6.58-6.60 (m, 2H), 7.00−7.34 (m, 14H), 10.42-10.53 (m, 4H), 10.71 (s, 1H) ppm.

(*E*) isomer: ^{1}H NMR (400 MHz, DMSO-d_6): δ = 5.28-5.31 (m, 2H), 5.46−5.56 (m, 4H), 5.63 (d, *J* = 16.4 Hz, 2H), 5.85−5.90 (m, 2H), 6.12 (s, 1H), 6.58-6.60 (m, 2H), 7.00−7.34 (m, 14H), 10.42-10.53 (m, 4H), 11.36 (s, 1H) ppm.

(*E*)- and (*Z*)-5,15-Diphenyl-10-[1-hydroxyimino-1-(*p*-bromophenyl)methyl]bilanes (17c)

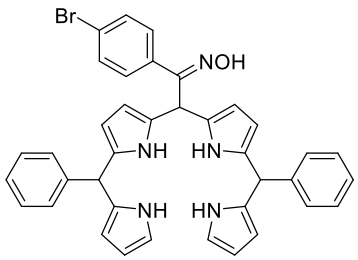

Compounds **17c** were obtained from oxime **15c** (1 mmol, 0.372 g) and dipyrromethane **16** (4 mmol, 0.889 g). Purification of the crude product by flash chromatography [ethyl acetate/hexane (1:2)] gave bilanes **17c** [Method A: 0.131 g, 20%, as a mixture of isomers *E*/*Z* (37:63); Method B: 0.216 g, 33%, as a mixture of isomers *E*/*Z* (56:44)] as a beige solid. HRMS (ESI-TOF) m/z: [M + H^{+}] calcd for $C_{38}H_{32}BrN_5O$, 654.1863; found, 654.1865.

(*Z*) isomer: ^{1}H NMR (400 MHz, DMSO-d_6): δ = 5.13 (s, 1H), 5.27-5.30 (m, 2H), 5.47−5.64 (m, 6H), 5.85−5.89 (m, 2H), 6.60 (s, 2H), 7.00−7.03 (m, 3H), 7.12-7.29 (m, 10H), 7.39-7.46 (m, 2H), 10.43-10.52 (m, 4H), 10.76 (s, 1H) ppm.

(*E*) isomer: ^{1}H NMR (400 MHz, DMSO-d_6): δ = 5.27-5.30 (m, 2H), 5.47−5.64 (m, 6H), 5.85−5.89 (m, 2H), 6.10 (s, 1H), 6.60 (s, 2H), 7.00−7.03 (m, 3H), 7.12-7.29 (m, 10H), 7.39-7.46 (m, 2H), 10.43-10.52 (m, 4H), 11.46 (s, 1H) ppm.

2.A.3.5. General procedure for synthesis of corroles:

DDQ (3 equiv, 0.3 mmol) was added to a solution of the appropriate bilane (0.1 mmol) in dry THF (20 mL). The mixture was stirred at room temperature for 3 hours, under an inert atmosphere. After this time, the mixture was concentrated under reduced pressure until it reached half the volume, and purified by flash chromatography [ethyl acetate/hexane (1:3)], followed by recrystallization in methanol.

5,15-Diphenyl-10-[1-hydroxyimino-1-(phenyl)methyl]corrole (18a)

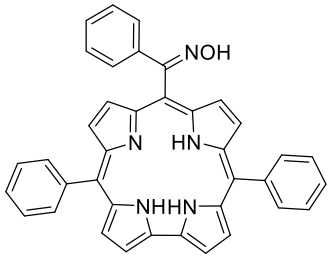

Compound **18a** was obtained from bilanes **17a** (0.140 g, 0.243 mmol) as a dark green solid (0.038 g, 27% yield). ^{1}H NMR (400 MHz, THF-d_8): δ = 7.19-7.26 (m, 4H), 7.65−7.80 (m, 8H), 8.33 (br s, 5H), 8.60 (d, *J* = 4 Hz, 2H), 8.74 (s, 2H), 8.87 (s, 2H), 10.53 (s, 1H) ppm; ^{13}C NMR (THF-d_8): δ = 98.6, 112.2, 112.7, 112.9, 123.1, 123.3, 125.2, 125.3, 125.9, 126.2, 133.0, 138.4, 138.9, 154.8 ppm; HRMS (ESI-TOF) m/z: [M + H^{+}] calcd for

$C_{38}H_{27}N_5O$, 570.2288; found, 570.2290; UV/vis λ_{abs} (DMSO, log ε) 417 (5.03), 431 (4.93), 581 (4.30), 611 (3.23), 648 (3.90).

5,15-Diphenyl-10-[1-hydroxyimino-1-(*p*-fluorophenyl)methyl]corrole (18b)

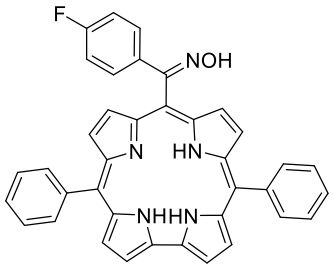

Compound **18b** was obtained from bilanes **17b** (0.189 g, 0.319 mmol) as a dark green solid (0.058 g, 31% yield). ^{1}H NMR (400 MHz, THF-d_8): δ = 6.96 (t, *J* = 16 Hz, 2H), 7.65-7.80 (m, 8H), 8.33 (br s, 6H), 8.58 (s, 2H), 8.75 (s, 2H), 8.88 (s, 2H), 10.57 (s, 1H) ppm; ^{13}C NMR (THF-d_8): δ = 98.2 112.6, 112.8, 125.2, 125.9, 127.1, 127.2, 133.0, 153.8, 159.6, 159.9 ppm; ^{19}F NMR (THF-d_8): δ = -116.8 ppm; HRMS (ESI-TOF) m/z: [M + H$^+$] calcd for $C_{38}H_{26}FN_5O$, 588.2194; found, 588.2176; UV/vis λ_{abs} (DMSO, log ε) 417 (4.73), 431 (4.64), 581 (4.98), 612 (3.91), 644 (3.74).

5,15-Diphenyl-10-[1-hydroxyimino-1-(*p*-bromophenyl)methyl]corrole (18c)

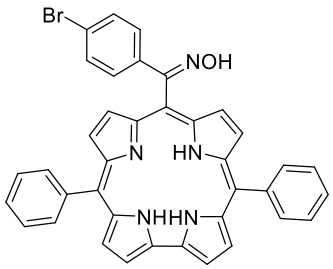

Compound **18c** was obtained from bilanes **17c** (0.216 g, 0.330 mmol) as a dark green solid (0.114 g, 53% yield). ^{1}H NMR (400 MHz, THF-d_8): δ = 7.37-7.45 (m, 3H), 7.61−7.69 (m, 4H), 7.79 (t, *J* = 16 Hz, 4H), 8.33 (s, 5H), 8.57 (s, 2H), 8.76 (s, 2H), 8.88 (s, 2H), 10.70 (s, 1H) ppm; ^{13}C NMR (THF-d_8): δ = 97.8, 112.7, 112.9, 120.4, 125.3, 125.9, 126.9, 129.1, 133.0, 138.1, 139.3, 154.0 ppm; HRMS (ESI-TOF) m/z: [M + H$^+$] calcd for $C_{38}H_{26}BrN_5O$, 648.1393; found, 648.1366; UV/vis λ_{abs} (DMSO, log ε) 418 (4.94), 432 (4.81), 581 (4.22), 612 (4.15), 644 (3.88).

Part B: *in vitro* assays

2.B.1. Cell Culture

Experiments were performed with two non-small cell lung carcinomas (NSCLC) cell lines: A549 (ATCC CCL-185® TM, adenocarcinoma, $P53^{Wild}$) and NCI-H1299/H1299 (ATCC CRL-5803® TM, large cell carcinoma, $P53^{Null}$).

The cell lines were cultured in Dulbecco's Modified Eagle's Medium (DMEM, Sigma D-5648) supplemented with 10% (A549) or 5% (H1299) fetal bovine serum (FBS, Sigma F7524), 100 µM sodium pyruvate (Gibco 11360), and 1 % antibiotic (100 U/mL penicillin and 10 µg/mL streptomycin; Gibco 1360), according to providers' recommendations and maintained at 37 °C in a humidified atmosphere with 95 % air and 5 % CO_2 in *Binder* incubator.

Cells form a monolayer, growing adherent to the solid support (flasks or cell culture plates). To carry out the *in vitro* studies these cells need to be transferred to suitable carriers, multiwell plates (MW), and enzymatic methods were used to prepare the cell suspensions. Thus, cell cultures were initially washed with a phosphate buffered saline (PBS), consisting of 137 mM NaCl (Sigma S7653), 2.7 mM KCl (Sigma P9333), 10 mM NaH_2PO_4 (Sigma S5011) and 1.8 mM KH_2PO_4 (Sigma P0662), pH was set at 7.4 and incubated at 37 °C with 3 mL of a trypsin-EDTA solution at 0.25 % (Sigma T4049) for the time required for the cells to detach from the flask. Thereafter, culture medium was added to inactivate the trypsin solution, the cell suspension was homogenized, and the cell concentration was determined. In this step, a known volume of cell suspension was diluted in equal volume of trypan blue and counted in an inverted microscope (Motic AE31), with a 10x magnification, using the hemocytometer (*Neubauer* chamber).[121] After counting, the volume of the cell suspensions was adjusted with culture medium, and cells were plated at an initial concentration of 0.2×10^6 cells/mL in 48-well plates (MW48), in order to maintain a constant number of 0.1×10^6 cells in a volume of 0.5 mL per well.

2.B.2. Photodynamic treatment

Corroles were solubilized in dimethylsulfoxide (DMSO, Fisher Chemical, 200-664-3), and eight stocks of defined concentrations in a range of 5 µM to 1 mM were prepared: 5 µM, 10 µM, 25 µM, 50 µM, 100 µM, 200 µM, 500 µM, and 1 mM. The concentration of all solutions of photosensitizers (PS) was adjusted, so that their addition only altered at most the volume of culture medium from the cell compartments by 1%, i.e. the volume of PS added was 5 µL. Tested concentrations ranged from 50 nM to 10 µM.

The cell cultures submitted to the photodynamic treatment were incubated for 24 hours with the desired PS concentrations. After this time, a wash was carried out with PBS, pH 7.4, which ensured that all the PS not internalized by the cells was removed, and 200 µL of culture medium was added to the cell compartments. In all studies the cultures were irradiated with a photon flux of 7.5 mW/cm^2 to a total of 10 J. Irradiation for photodynamic treatment was performed using a fluorescent light source equipped with a red filter ($\lambda_{cut\ off}$ < 560 nm). The evaluations were performed 24 hours after the photodynamic treatment.

2.B.3. Photocytotoxicity and dark cytotoxicity

The cell cultures not submitted to the photodynamic treatment (dark cytotoxicity assays) were incubated for 24 hours with the desired PS concentrations. Then, a wash was carried out with PBS, 200 µL of culture medium was added to the cell compartments, and cells were incubated for 24 hours before metabolic activity assessment.

To evaluate the effect of the corroles on the metabolic activity of the cells, the MTT (3-(4,5-dimethylthiazol-2-yl)-2,5-diphenyltetrazolium bromide) assay was performed. MTT is reduced by metabolically active cells due to the action of dehydrogenase enzymes, mainly through the action of complex II of the mitochondrial respiratory chain, succinate dehydrogenase or succinate-coenzyme Q reductase. The dehydrogenases have the ability to cleave the MTT tetrazolium rings and form dark blue formazan crystals, which can be subsequently solubilized and quantified by spectrophotometric means. Thus, the amount of formazan crystals obtained is directly proportional to the mitochondrial cell function, and consequently to the metabolic activity of the cells.[122]

The cell suspensions of A549 and H1299 were distributed into 48-well plates. These plates were incubated overnight to allow cell adhesion. PSs were administered in concentrations ranging from 50 nM and 10 µM. In all assays six PS concentrations, and two controls (untreated cell cultures and cell cultures subjected DMSO which is the PS delivery vehicle) were performed in triplicate. Metabolic activity analysis was performed 24 hours after the photodynamic treatment.

For the MTT assay procedure, the cell culture medium was aspirated and washed with PBS from each well. Subsequently, 100 µL of a solution of MTT (0.5 mg/mL; Sigma M5655) in PBS, pH 7.4, was placed in each well and incubated in the dark at 37 °C for 4 hours. To solubilize the obtained formazan crystals, 100 µL of a 0.04 M solution of hydrochloric acid (Merck Millipore 100317) in isopropanol (Sigma 278475) was added to each well and the plates allowed to stir until complete dissolution. The absorbance was

quantified at 570 nm with a reference filter of 620 nm using the EnSpire Multimode Plate Reader.

Dark cytotoxicity studies were performed without the step of irradiation, as described previously.

The metabolic activity was expressed as a percentage of the metabolic activity of the cultures submitted to the photodynamic treatment in relation to the metabolic activity of the cultures treated with the sensitizer administration vehicle alone, using the equation below, where Abs corresponds to the absorbance.

$$Metabolic\ activity\ (\%) = \frac{Treated\ cells\ (Abs\ 570 - Abs\ 620)}{Control\ cells\ (Abs\ 570 - Abs\ 620)} \times 100$$

This procedure allowed to establish dose-response curves and to determine the concentration of the sensitizers that inhibits the metabolic activity of the cultures in 50 % (IC_{50}). The obtained results were analyzed, processed in the program GraphPad Prism 7 and adjusted to a sigmoid curve according to the equation:

$$Metabolic\ activity = \frac{100}{1 + e^{(logx_0 - logC) \times s}}$$

Where C is the concentration, s is the slope of the central region of the sigmoid and x_0 is the IC_{50}. The 95 % confidence intervals for the IC_{50} were obtained from the parameters obtained by curve fitting (log x_0 and respective standard error).

2.B.4. Cell viability

The sulforhodamine B (SRB) assay allows assessment of cell viability by correlation with total protein content. Sulforhodamine B is a purplish, anionic and pH dependent dye, with affinity for amino acids, to which it binds electrostatically. Under acidic conditions, it binds to the amino acids of cellular proteins and, under alkaline conditions, can be extracted. After fixation, solubilization and measurement by spectrophotometric methods, the results obtained correlate with the number of cells through total protein content.[123,124]

Corroles (**18a-c** and **22a-d**) were administered at concentrations of 50 nM, 100 nM and 500 nM. In each study two controls were performed, one with untreated cells and the other with DMSO. Photodynamic treatment was performed as described above, and the SRB assay was performed 24 hours after irradiation.

For the SRB assay, 200 µL of acetic acid 1% (Honeywell 33209) in methanol (Fisher Chemical M/4000/PC17) were added and incubated for 1 hour at 4 °C. After this time, the supernatant was discarded and 200 µL of SRB at 0.5% (Sigma S9012) dissolved in 1% acetic acid (Honeywell 33209) in H_2O were added to each well and plates were stored for 1 hour and 30 minutes in the dark. After this time, the plates were washed to remove excess SRB and, after drying the plate, 200 µL of TRIS-NaOH (pH 10) (Sigma T1503) were added. Absorbance reading was done at wavelength 540 nm, with a reference filter of 690 nm, in EnSpire Multimode Plate Reader. The results were expressed as percentage of the protein content of the cultures submitted to the photosensitizer in relation to the protein content of the cultures treated only with the sensitizer delivery vehicle (DMSO).

Chapter 3: Results and Discussion

This chapter is divided into two parts. In **Part A** the results on the synthesis of *trans*-A_2B-corroles (Figure 10). In this part were also described the synthesis of α,α-dibromoketones, oximes and dipyrromenthanes in order to obtained bilanes, precursors of the desired corroles. Furthermore, the photophysical and photochemical characterization of the synthesized corroles is demonstrated.

In **Part B** the photocytotoxicity and dark cytotoxicity of the corroles synthesized in Part A and more four corroles previously synthesized in the Organic Chemistry Group is presented and discussed.

Chapter 3.A: Chemical synthesis and characterization

3.A.1. Introduction

Lopes and Pinho e Melo described a novel approach to *trans*-A_2B-corroles based on the reactivity of nitrosoalkenes towards dipyrromethanes (Scheme 1). The synthetic strategy, involves the synthesis of bilanes **21** from α,α-dihalo-oximes **19** and dipyrromethanes **20** either via bis-hetero-Diels-Alder reaction or conjugate addition, followed by an oxidative macrocyclization to afford a new class of *trans*-A_2B-corroles **22**.[116]

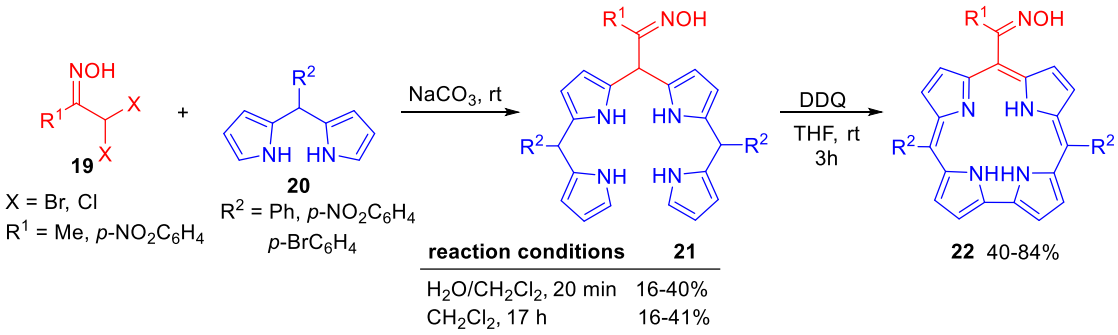

reaction conditions	21
H_2O/CH_2Cl_2, 20 min	16-40%
CH_2Cl_2, 17 h	16-41%

Scheme 1: Synthesis of bilanes **21** and *trans*-A_2B-corroles **22**.

The chemical behavior of nitrosoalkenes generated *in situ* from the oximes toward dipyrromethanes is strongly dependent on the nature of the 3- and/or 4-substituents.[116,125–128] Pinho e Melo and coworkers observed that 1-methylnitrosoethylenes (generated *in situ* from methyloximes) react with dipyrromethanes via hetero-Diels-Alder reaction, affording products as single oximes, whereas 1-arylnitrosoethylenes (generated *in situ* from aryloximes) react through conjugate addition or via hetero-Diels-Alder reaction affording two isomeric oximes.[116] Interestingly, an easy and unambiguous way to determine the mechanism pathway involved in the synthesis of bilanes is the outcome of the reaction regarding the selectivity of oxime formation, single stereoisomer versus *E*/*Z* mixtures.

In this context, the two possible mechanisms for the synthesis of bilanes from nitrosoalkenes and dipyrromethanes are outlined in Scheme 2. Dehydrohalogenation of the starting α,α-dihalo-oximes **19** in the presence of sodium carbonate generates the transient α-halo-nitrosoalkenes **23**, which reacts with the first molecule of the appropriate dipyrromethane **20** either via hetero-Diels−Alder reaction (when R^1 = Me, Aryl), or conjugated addition followed by [1,5]hydrogen shift (when R^1 = Aryl) to give the corresponding alkylated dipyrromethanes **24**. The side chain of this functionalized DP can undergo another dehydrohalogenation to afford a new nitrosoalkene **25**, which reacts with the second molecule of dipyrromethane **20** to give the expected bilanes **21**.

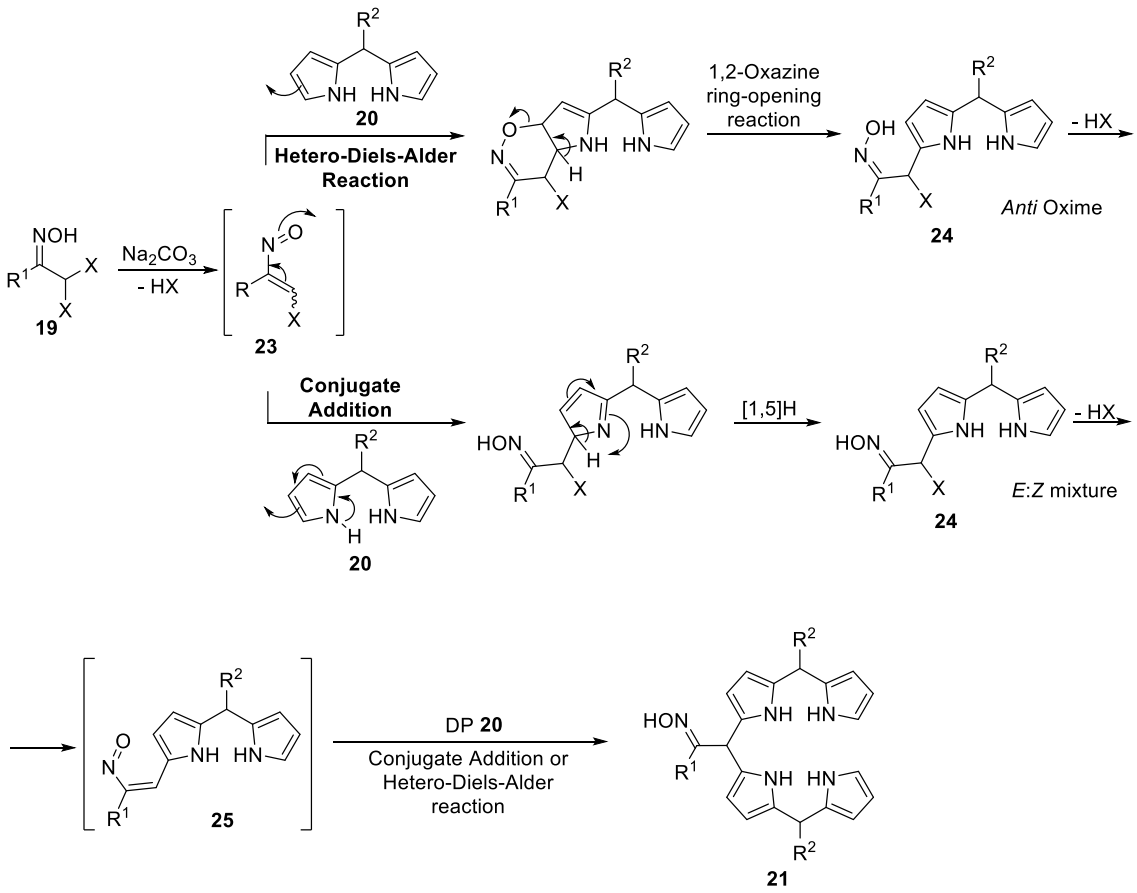

Scheme 2: Mechanism proposal for the synthesis of oxime-containing bilanes based on the reactivity of nitrosoalkenes toward dipyrromethanes.

In this project, three new *trans*-A_2B-corroles were synthetized and its photophysical characterization were performed together with corroles previously synthesized by Lopes.[116]

3.A.2. Synthesis of bilanes and corroles

The oxime precursors - α,α-dibromoketones **14** - were synthesized by bromination of the corresponding ketone **26** using 2 equiv of bromine in glacial acetic acid (Scheme 3), according to a procedure described in the literature.[117,118] α,α-Dibromoketones **14** were obtained in high yields (66-78%).

The synthesis of the oximes **15** resulted from the reaction of the corresponding α,α-dibromoketone **14** with hydroxylamine hydrochloride in ethanol at room temperature (Scheme 2), according to a procedure described in the literature.[119] The oximes containing three distinct substituents, a phenyl group **15a**, a phenyl group with a fluorine in the *para* position **15b**, and a phenyl group with a bromine in the *para* position **15c** were obtained in 60%, 36% and 51% yield, respectively.

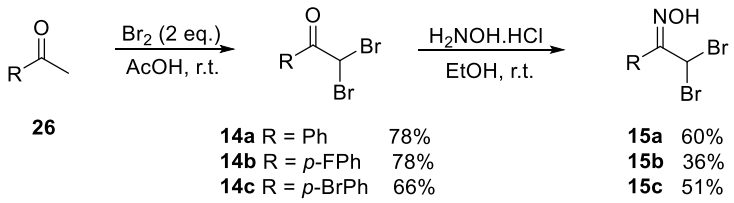

Scheme 3: Synthesis of α,α-dibromoketones **14** and α,α-dibromo-oximes **15**.

Dipyrromethane **16** resulted from the trifluoroacetic acid catalyzed condensation of benzaldehyde (**27**) with pyrrole (**28**) at room temperature (Scheme 4), according to a procedure described in the literature.[120] Dipyrromethane **16** containing a phenyl group (Ph) in *meso* position was obtained in 53% yield.

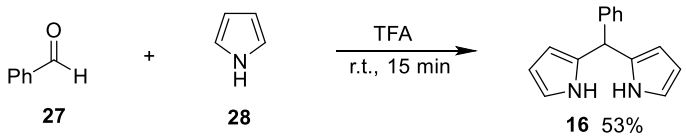

Scheme 4: Synthesis of dipyrromethane **16**.

Bilanes **17** resulted from the reaction of nitrosoalkenes generated *in situ* from dehydrohalogetion of α,α-dibromo-oximes **15**, with dipyrromethane **16** (1:4 oxime/DP ratio) in the presence of sodium carbonate, in two different methodologies. In method A, solvent system water/dichloromethane (H_2O/CH_2Cl_2, 85/15) was used, and the mixture was stirred at room temperature for 20 minutes. In method B, dichloromethane was used as solvent, and the mixture was stirred at room temperature for 17 hours.

The synthetic strategy, reactions yields and isomeric proportions of bilanes **17** are summarized in table 3. Bilane **17a** was obtained in 25% yield using the H_2O/CH_2Cl_2 solvent system (entry 1), and 33% yield carrying out the reaction in dichloromethane (entry 2). Bilane **17b** was obtained in 32% yield using the H_2O/CH_2Cl_2 solvent system (entry 3), and in dichloromethane (entry 4). Bilane **17c** was obtained in 25% yield using the H_2O/CH_2Cl_2 solvent system (entry 5), and 33% yield carrying out the reaction in dichloromethane (entry 6).

On-water reactions are particularly interesting not only in the context of the development of a more sustainable methodology but because they are much faster and can lead to different reactivities and selectivities in similar yields. In fact, reactions using the H_2O/CH_2Cl_2 solvent system generate mostly *Z*-isomer, whereas reactions in dichloromethane generate mostly *E*-isomer, as shown in table 3.

Table 3: Synthesis of bilanes **17**.

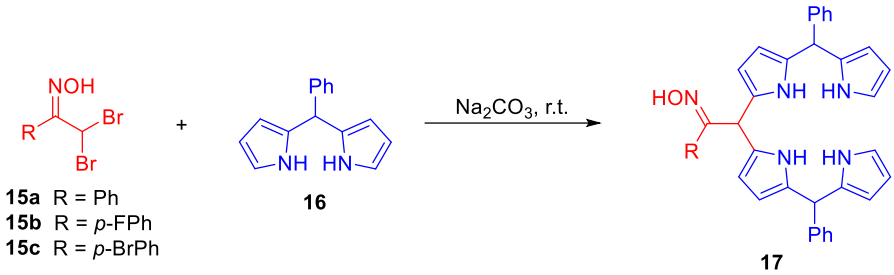

15a R = Ph
15b R = *p*-FPh
15c R = *p*-BrPh

16

17

Entry	Oxime	Reaction conditions	Yield (*E*:*Z*)
1	**15a**	H_2O/CH_2Cl_2, 20 min	**17a** 25% (40:60)
2	**15a**	CH_2Cl_2, 17 h	**17a** 33% (58:42)
3	**15b**	H_2O/CH_2Cl_2, 20 min	**17b** 32% (33:67)
4	**15b**	CH_2Cl_2, 17 h	**17b** 32% (51:49)
5	**15c**	H_2O/CH_2Cl_2, 20 min	**17c** 20% (38:62)
6	**15c**	CH_2Cl_2, 17 h	**17c** 33% (56:44)

In all cases, bilanes **17** were isolated as a mixture of *E* and *Z* isomeric oximes. Based on ^{1}H NMR spectrum, the configuration of the oxime group could be assigned. The figure 11 shows the differences in the structure and in the ^{1}H NMR spectrum of bilanes **17c**, where the *meso*-proton (in blue) and the proton of hydroxyl group (in red) of the bilane bearing a *Z*-oxime appear at a lower chemical shift than the values observed for the derivative with the *E*-oxime.

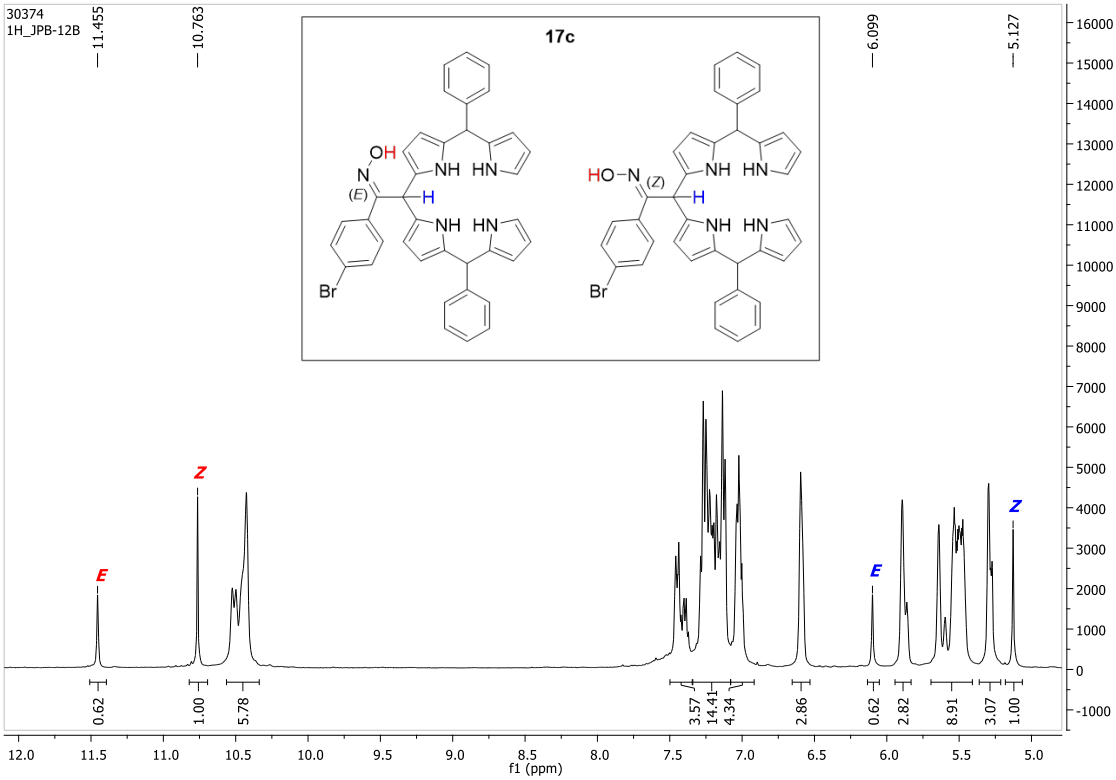

Figure 11: ^{1}H NMR spectrum of the two stereoisomers (*E*)- and (*Z*)- bilanes **17c** obtained using the H_2O/CH_2Cl_2 solvent system.

As with other arylnitrosoalkenes, a mixture of stereoisomers *E*/*Z* was also observed and therefore these reactions follow the mechanism shown in scheme 2 (page 45) of this thesis). Thus, we can conclude that bilanes result from the reaction between nitrosoalkenes and dipyrromethane via two consecutive hetero-Diels-Alder reactions or via conjugated additions.

The oxidative macrocyclization of bilanes **17** to the corresponding corroles **18** was performed using 2,3-dichloro-5,6-dicyano-*p*-benzoquinone (DDQ) as oxidant. Corroles **18a**, **18b** and **18c** were obtained in 27%, 31% and 53% yield, respectively.

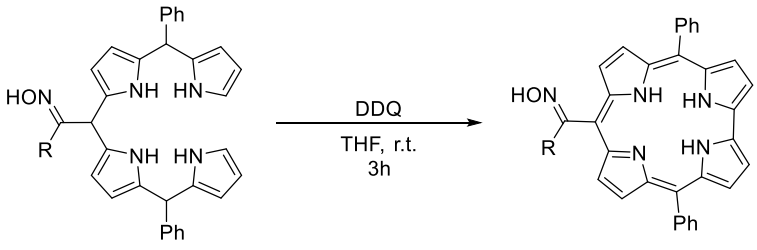

18a R = Ph 27%
18b R = *p*-BrPh 31%
18c R = *p*-FPh 53%

Scheme 5: Synthesis of *trans*-A_2B-corroles **18**.

Photophysical characterization of the three newly synthesized *trans*-A_2B-corroles were studied together with corroles previously synthesized by Lopes,[116] which structure are presented in figure 12.

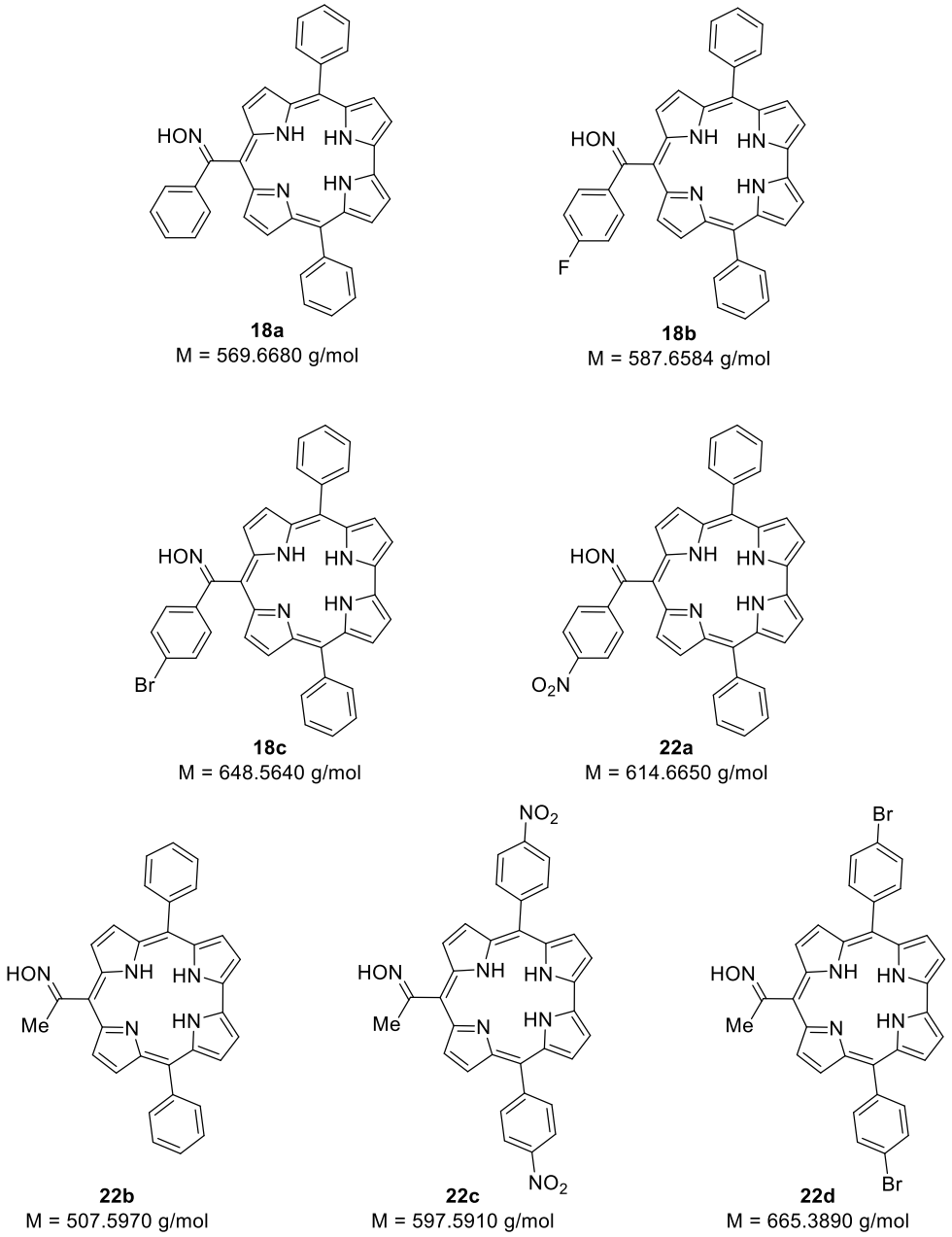

Figure 12: Structures of all *Trans*-A_2B-corroles studied.

3.A.3. Photophysical characterization of *trans*-A_2B-corroles

The compounds presented in this dissertation were also characterized by molecular absorption spectroscopy. This technique provides important information for the possible application of the compounds as PS, since the molecules must have some specific characteristics.

On an absorption spectrum, free base corroles have a band with a high absorption coefficient in the near ultraviolet (around 400 nm), called Soret or B band, and a series bands of lower absorption coefficient (Q bands), which are located in the visible region (between 500 and 700 nm). The absorption spectrum of corroles could be interpreted with the four-orbital model proposed by Gouterman.[129,130] The number and Shape of the Q bands is highly influence by the substituents.

The normalized absorption spectra of corroles with methyl oxime group at the *meso* position 10 – corroles **22b**, **22c** and **22d** – are presented in Figure 13.

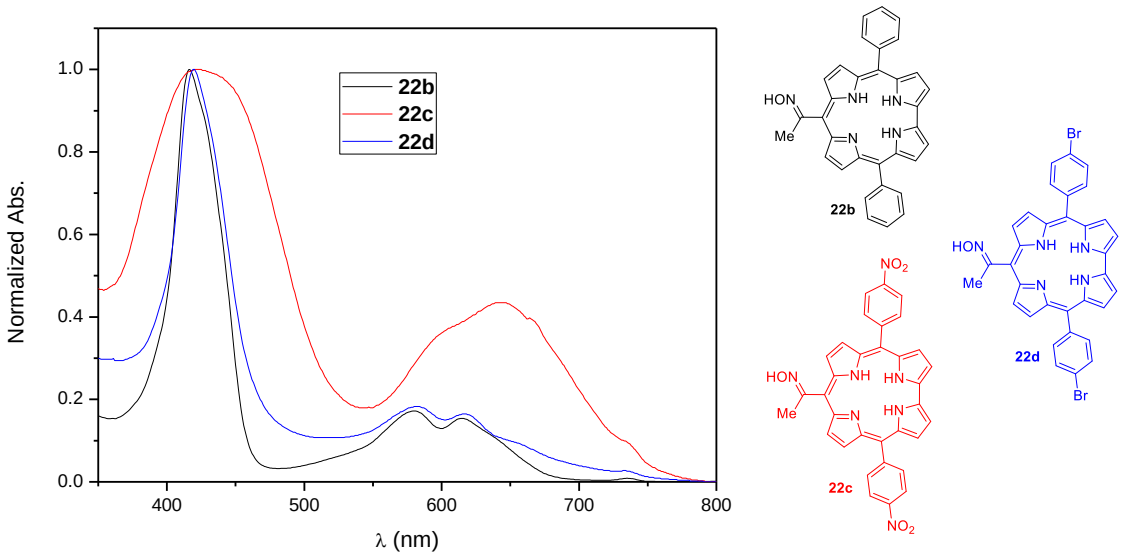

Figure 13: Normalized absorption spectra of corroles with methyloxime at the *meso*-position.

The absorption spectra of this type of corroles is greatly influenced by the substituents at the 5 and 15 position. Corroles with substituents phenyl (**22b**) and bromophenyl (**22d**) present a Soret Band at 420 nm and Q bands at 580-665 nm region. The corrole with phenyl substituent present two Q bands while the corrole with the bromine atoms shows three Q bands at 583, 618 and 664 nm. The nitro group at the phenyl ring (**22c**) change the shape of the UV-vis spectrum that present two broad bands at 428 and 641 nm with absorption coefficients of 104 M^{-1} cm^{-1} (Table 4).

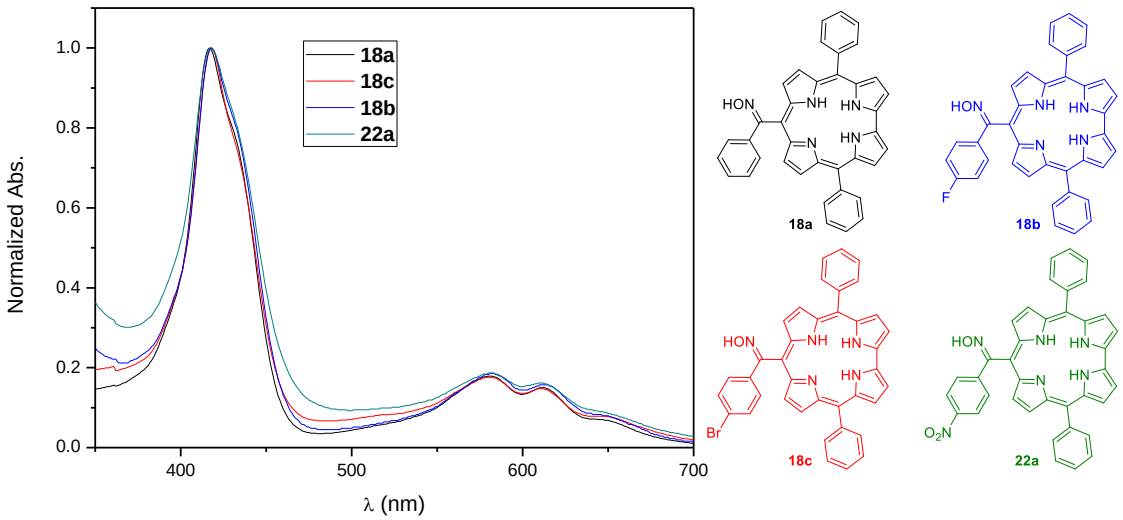

Figure 14: Normalized absorption spectra of corroles with phenyloxime at the *meso*-position.

The corroles with phenyl oxime substituents – corroles **18a**, **18b**, **18c** and **22a** – show a UV-Vis absorption spectra very similar with a Soret band at 417-418 nm, which present a shoulder at 431-432 nm, and three Q bands at 581, 611 and 645 nm. Clearly, the substituents at the phenyloxime group have a small influence in the absorption characteristics of these compounds, Figure 14.

The wavelength of the maxima absorption and the absorption coefficients calculated using solutions of concentration between $2x10^{-5}$ and $4x10^{-6}$ M in DMSO at room temperature are presented at Table 4. Using the Beer-Lambert law (A=εbc, where A is the absorbance, ε is the molar absorptivity coefficient, b is the optical path travelled by light and c is the concentration of solution), absorption as a function of concentration is plotted on a graph. The slope of the adjusted line determines the molar absorptivity coefficient (ε) for Q and Soret bands. Correlation coefficients obtained for the straight lines were high and, in the range of the concentrations used, we did not find any deviation to Beer-Lambert law ($R^2 > 0.99$), which indicates the absence of aggregation of the compounds in the range of concentration and with the solvent studied.

Contrary to porphyrins, where aggregation have been deeply investigated, the aggregation of corroles has been less explored.[94] In porphyrins, the aggregation causes a decrease in the lifetime of singlet and triplet states of the PS, that leads to a decrease in the quantum yields of singlet oxygen, which ultimately decreases the photodynamic efficiency of the PS. However, in corroles this correlation does not seem to be observed. Recent studies show that the aggregation of these macrocycles increases absorption in the therapeutic window, enhancing their applicability in PDT.

Table 4: Wavelength of the maxima of the absorption coefficients of corroles in this study.

Corrole		Soret	Soret (sh)	Q-bands λmax (nm), ε ($M^{-1}cm^{-1}$)		
18a	λmax (nm)	417	431	581	611	648
	ε ($M^{-1}cm^{-1}$)	$1.07x10^5$	$8.45x10^4$	$1.99x10^4$	$1.68x10^3$	$7.92x10^3$
18b	λmax (nm)	417	431	581	612	644
	ε ($M^{-1}cm^{-1}$)	$5.36x10^4$	$4.36x10^4$	$9.52x10^4$	$8.12x10^3$	$5.45x10^3$
18c	λmax (nm)	418	432	581	612	644
	ε ($M^{-1}cm^{-1}$)	$8.64x10^4$	$6.52x10^4$	$1.67x10^4$	$1.42x10^4$	$7.58x10^3$
22a	λmax (nm)	417	431	581	611	644
	ε ($M^{-1}cm^{-1}$)	$6.32x10^4$	$5.32x10^4$	$1.32x10^4$	$1.16x10^4$	$6.94x10^3$
22b	λmax (nm)	417	-	579		613
	ε ($M^{-1}cm^{-1}$)	$1.12x10^5$	-	$1.87x10^4$		$1.70x10^4$
22c	λmax (nm)	428	-	641		
	ε ($M^{-1}cm^{-1}$)	$4.24x10^4$	-	$1.89x10^4$		
22d	λmax (nm)	421	-	583	618	664
	ε ($M^{-1}cm^{-1}$)*	$5.7x10^4$	-	$9.8x10^3$	$9.3x10^3$	$4.4x10^3$

* Minus a significant figure because there is a greater error in the measurement.

Solvent used: DMSO.

Chapter 3.B: Cell biology studies

3.B.1. Photocytotoxicity and dark cytotoxicity

The seven corroles were tested in order to assess their potential use as photosensitizers in PDT. For this, MTT assays were performed to evaluate photocytotoxicity and cytotoxicity of the compounds in two lung cancer cell lines (A549 and H1299). This technique is very useful for rapid screening of various compounds since it provides an indication of the metabolic state, with the main contribution of mitochondrial enzymes.[131] Therefore, the reduction of MTT is influenced not only by viability, but also by several factors intrinsic to the metabolism itself.[132]

The results obtained by the MTT assay after 24 hours of photodynamic treatment for the seven corroles were adjusted to a sigmoid dose-response model. In Figure 15.A and 15.B are represented the dose-response curves of the H1299 and the A549 cell lines, respectively. From the equation of each curve the mean point, corresponding to the IC_{50} value, was calculated and presented in Table 5, together with respective 95% confidence intervals and R^2 of the curves.

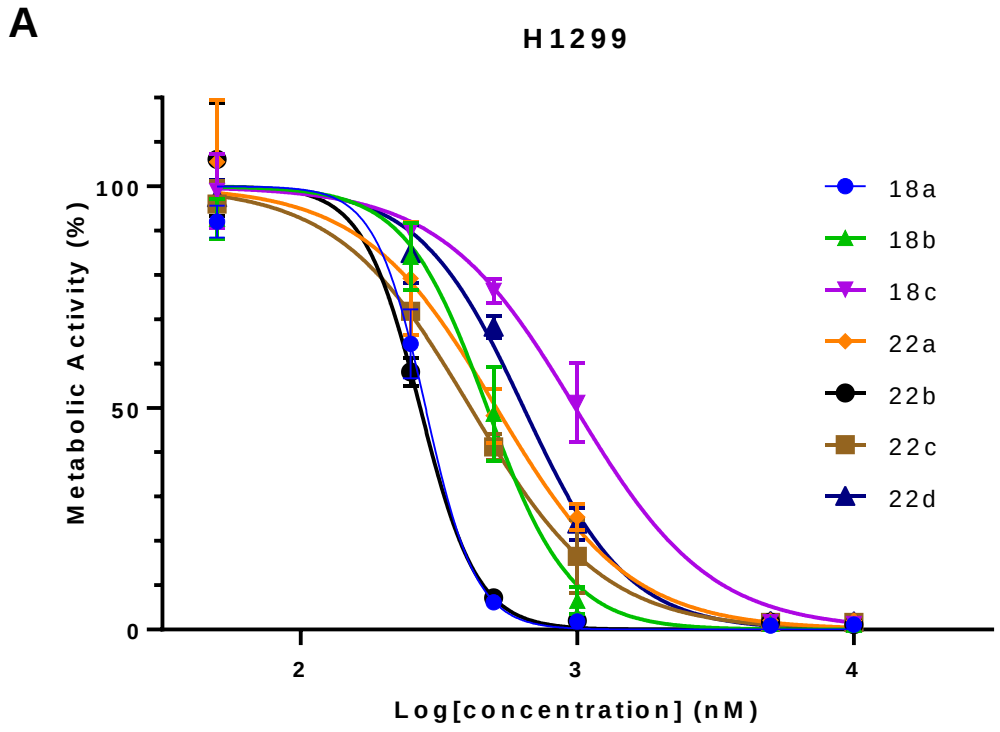

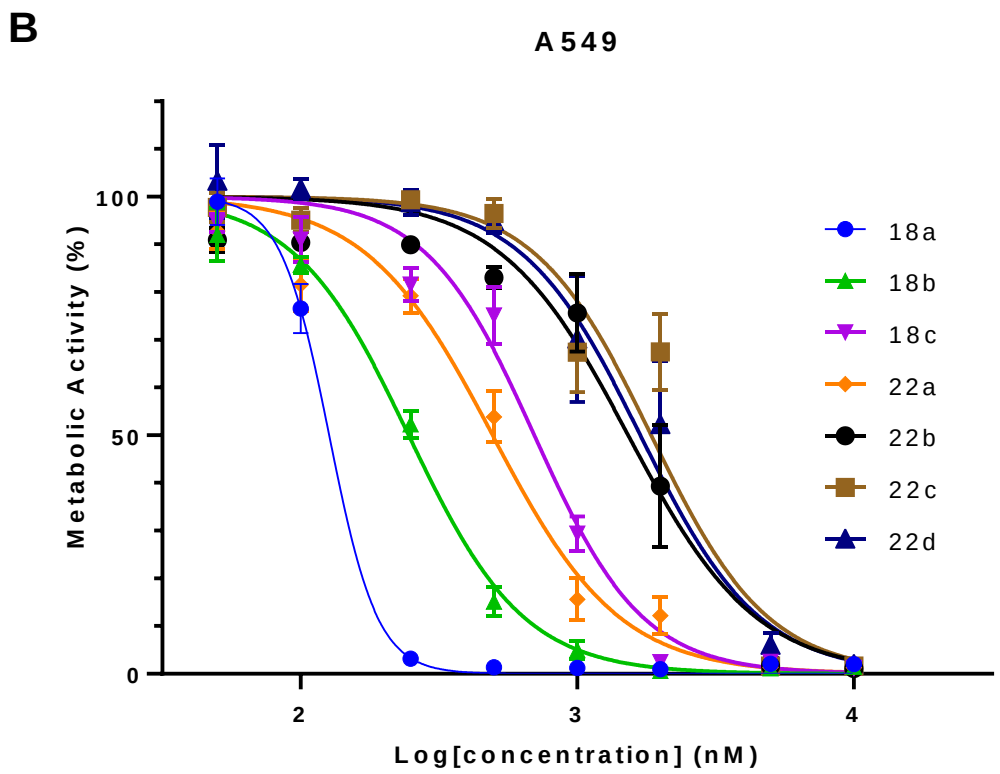

Figure 15: Dose-response curves for corroles submitted to irradiation in: A) H1299 cell line; B) A549 cell line. Results are presented as mean ± SD (at least n = 6).

Table 5: IC_{50} levels of the seven corroles in human lung carcer cell lines H1299 and A549, 24 hours after photodynamic treatment.

Compound	H1299			A549		
	IC_{50} (nM)	$CI_{95\%}$ (nM)	R^2	IC_{50} (nM)	$CI_{95\%}$ (nM)	R^2
18a	283.3	< 306.3	0.9640	126.8	< 137	0.9642
18b	473.5	[410.0; 543.0]	0.9487	246.0	[219.7; 272.9]	0.9729
18c	985.5	[831.0; 1195]	0.9651	700.4	[624.0; 781.2]	0.9595
22a	510.6	[396.7; 665.3]	0.9093	494.4	[431.8; 561.3]	0.9391
22b	270.6	[243.9; 301.5]	0.9440	1530	[1292; 1828]	0.9223
22c	412.3	[361.7; 467.4]	0.9595	1853	[1522; 2267]	0.9353
22d	640.7	[575.8; 713.8]	0.9765	1693	[1335; 2200]	0.8761

Considering the results in their entirety, it is verified that A549 cell line apparently presents a greater sensitivity to the compounds with phenyl oxime substituents (corroles **18a-c** and **22a**). Nevertheless, for the H1299 cell line, the most promising compounds

appear to be those with the lowest molecular weight (corroles **18a** and **22b**), opposing to those with the highest molecular weight (corroles **22d** and **18c**).

As the IC_{50} values obtained with the photosensitizers are very promising (most in the order of nanomolar), dose-response curves and IC_{50} of the most promising corrole (**18a**) was compared with a clinical approved PS which have been evaluated by the same methodology for A549 cell line. Figure 16 presents the corrole 18a in comparisom with 5,10,15,20-tetra(*m*-hydroxyphenyl)chlorin (*m*THPC) with the generic name ‘‘Temoporfin’’ and the proprietary name ‘‘Foscan®’’.

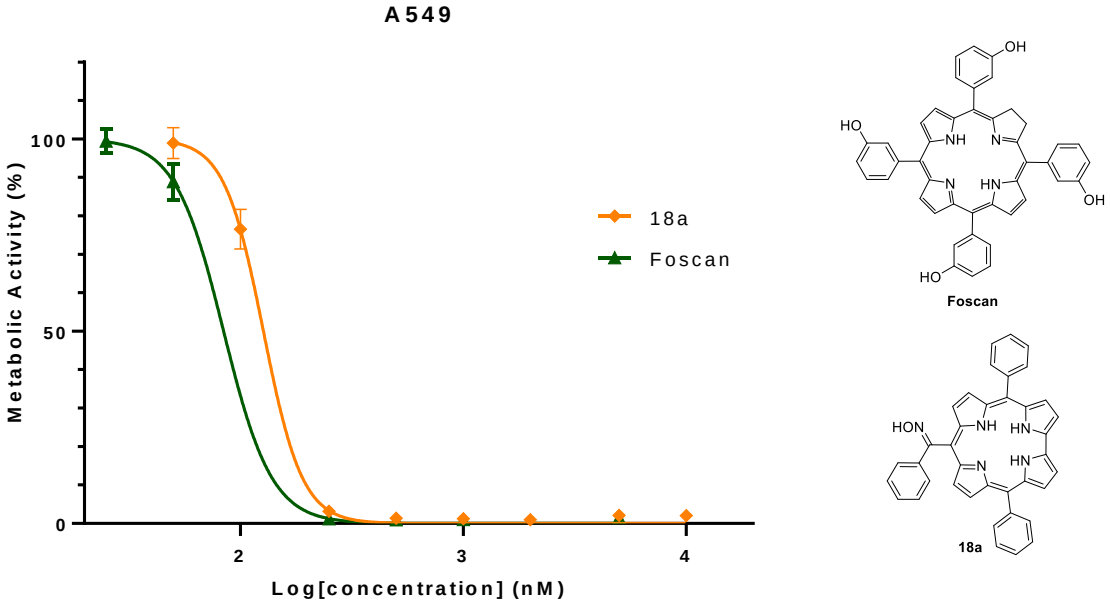

Figure 16: Dose-response curves for corrole **18a** and Foscan® in A549 cell line. Results are presented as mean ± SD (at least n = 4).

Despite the visible differences, IC_{50} of the Foscan® and corrole **18a** are both in nanomolar range (84.09 and 126.8 nM, respectively). Table 6 shows the respective 95% confidence intervals that prove the absence of significant differences between the compounds.

Table 6: IC_{50} levels with respective 95% confidence intervals and R^2 of Foscan® and corrole **18a** in A549 cell line.

Compound	A549		
	IC_{50} (nM)	**$CI_{95\%}$ (nM)**	**R^2**
18a	126.8	< 137	0.9881
Foscan®	84.09	< 102	0.9915

Metabolic activity studies of the cell cultures not submitted to the photodynamic treatment (dark cytotoxicity assays) were also made. Figure 17 shows the values of metabolic activity for the two highest tested concentrations of each sensitizer in H1299 and A549 cell lines. Up to a concentration of 5 µM, none of the compounds was significantly cytotoxic. At 10 µM, corrole **22c** was able to reduce cell viability in H1299 and A549 cell lines to 40.2% and 69.8%, respectively. This cytotoxicity may be related to the presence of nitro groups, and not necessarily to the photophysical characteristics of the macrocycle. The other corroles revealed not to be cytotoxic even at the higher concentration, when not irradiated.

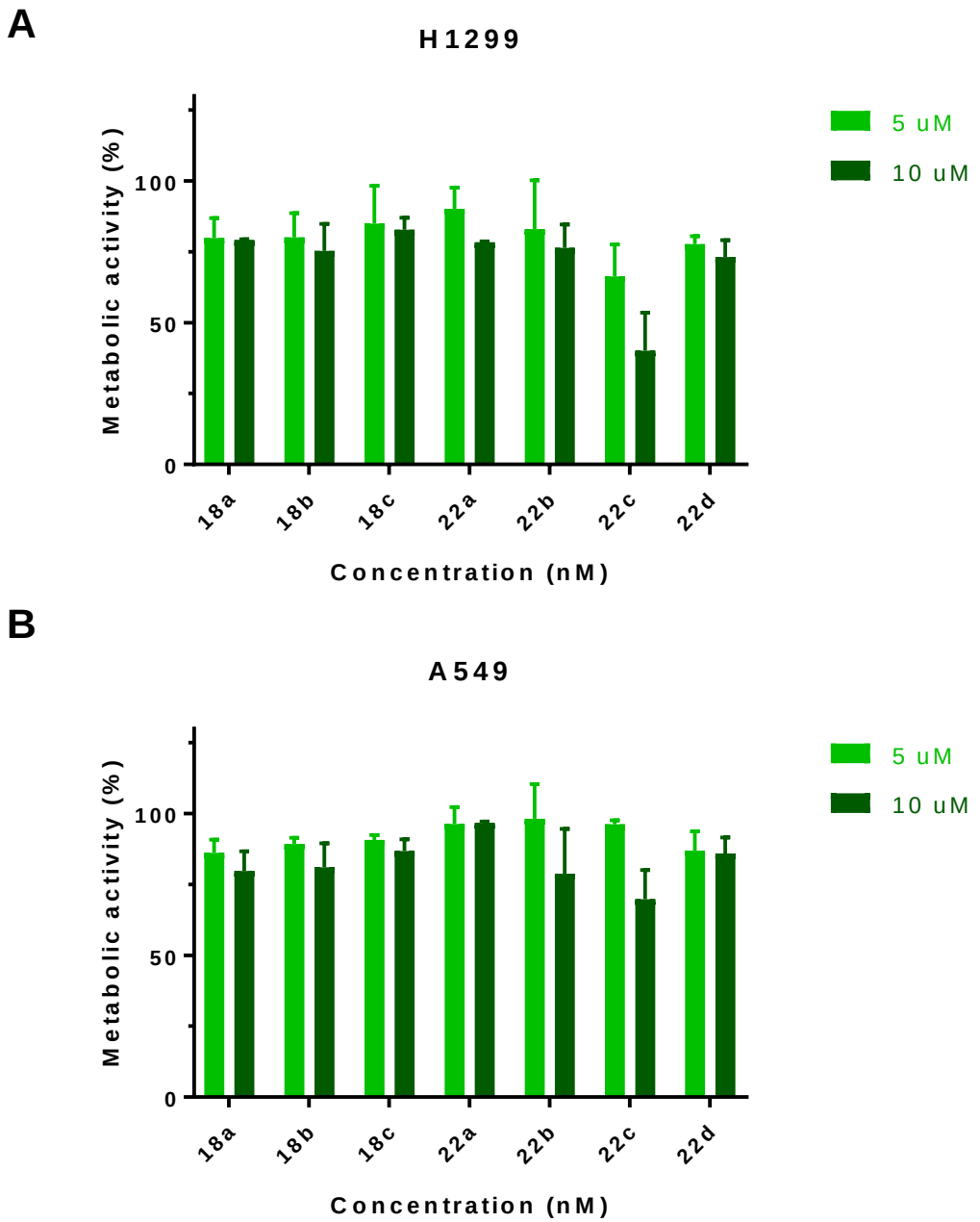

Figure 17: Metabolic activity of cell treated with corroles not submitted to irradiation in: A) H1299 cell line; B) A549 cell line. Results are presented as mean ± SD (at least n = 2).

3.B.2. Cell viability

In a complementary manner, cell viability with photosensitizers **18a-c** and **22a-d** was studied in H1299 and A549 cell lines 24 hours after photodynamic treatment, and compared to viability of the cells submitted to the sensitizers in the same concentrations, but without irradiation. To achieve this goal, the SBR assay, which is an indication of the change in total protein content and therefore correlates with cell biomass,[2] was used. Figure 18 and Figure 19 presents the results obtained in H1299 and A549 cell lines, respectively.

Figure 18 shows the viability of the H1299 cell cultures was significantly reduced after photodynamic treatment with the *trans*-A_2B-corroles studied. Unsurprisingly, there was no decrease in viability of cells exposed to sensitizers, but not irradiated. The corroles with phenyl oxime substituents at the *meso* position 10 – corroles **18a-c** and **22a** – presented the most promising results. Corrole **18a** showed the best results, managing to reduce cell viability to less than 50% even at the lowest concentration (50 nM). Corrole **18b** also proved to be very promising, managing to reduce cell viability to less than half at the concentration of 100 nM. Corroles **18c** and **22a** needed concentrations in the order of 250 nM to reduce cell viability to less than 50%. On the other hand, the corroles with methyl oxime group at the *meso* position 10 – corroles **22b-d** – presented the less promising results. In fact, corrole **22b**, which had shown the most promising results in metabolic activity in the H1299 cell line, fell short of expectations in cell viability assays, having halved cell viability only at the highest concentration (500 nM). Corroles **22c**, and **22d** also only managed to reduce cell viability to values below 50% at the highest concentration (500 nM).

These results corroborate those previously obtained in the metabolic activity for the group of corroles with phenyl oxime substituents at the *meso* position 10 (**18a-c** and **22a**), but are disappointing for the group of corroles with methyl oxime group (**22b-d**).

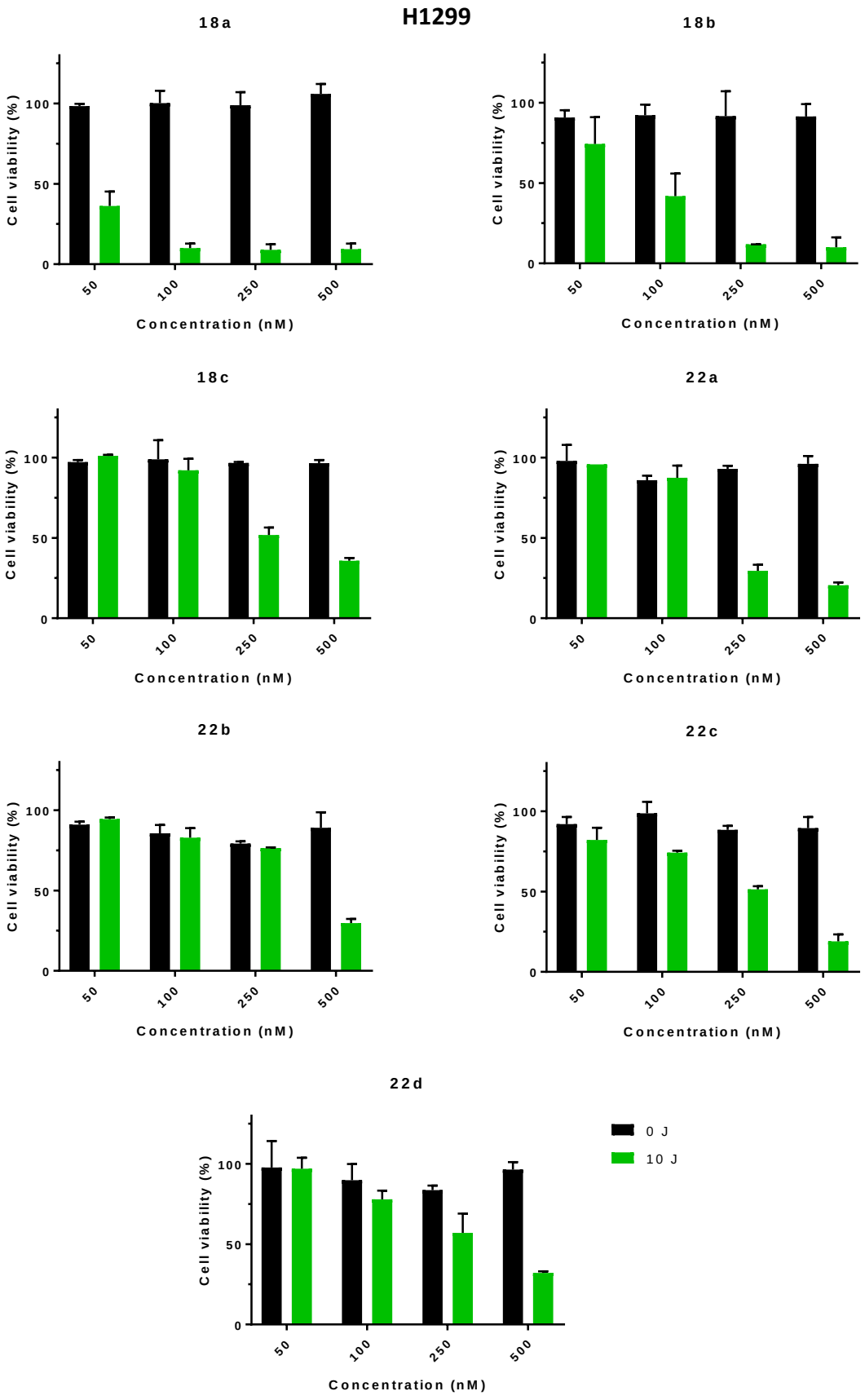

Figure 18: Cell viability of H1299 cell line 24 hours after the photodynamic treatment (10 J) and without irradiation (0 J) based on four sensitizers concentrations. Results are presented as mean ± SD (at least n = 2).

Figure 19 presents the viability of the A549 cell cultures was also significantly reduced after photodynamic treatment with the *trans*-A_2B-corroles studied. Unsurprisingly, there was no decrease in viability of cells exposed to sensitizers, but not irradiated. Like the previously described results for the H1299 cell line, the corroles with phenyl oxime substituents at the *meso* position 10 – corroles **18a-c** and **22a** – presented the most promising results for A549 cell line. Corrole **18a** showed the best results, managing to reduce cell viability to less than 50% even at the lowest concentration (50 nM). Corroles **18b** and **18c** were able to cause a significant decrease in cell viability to 30% and 27% respectively, when at concentrations of 500 nM. Although less expressive, corrole **22a** also managed to lower cell viability to values close to 50% when the concentration was 500 nM. On the other hand, the corroles with methyl oxime group at the *meso* position 10 – corroles **22b-d** – presented the less promising results. In fact, none of them was able to lower cell viability below 50% in the range of concentrations studied.

These results corroborate those previously obtained in the metabolic activity for all corroles studied.

The absence of cytotoxicity, combined with photocytotoxicity values in the nM range, and corroborated with cell viability decreased, supports the hypothesis that *trans*-A_2B-corroles have enormous potential for photodynamic therapy of lung cancer. Corrole **18b** showed to be the most promising sensitizer, and the phenyl substituent at the oxime group of the sensitizer has been shown to play a decisive role in the photodynamic activity of *trans*-A_2B-corroles. Molecular weight also appears to affect photodynamic activity, with the lighter compounds showing more promising results than the heavier compounds, within each of the groups.

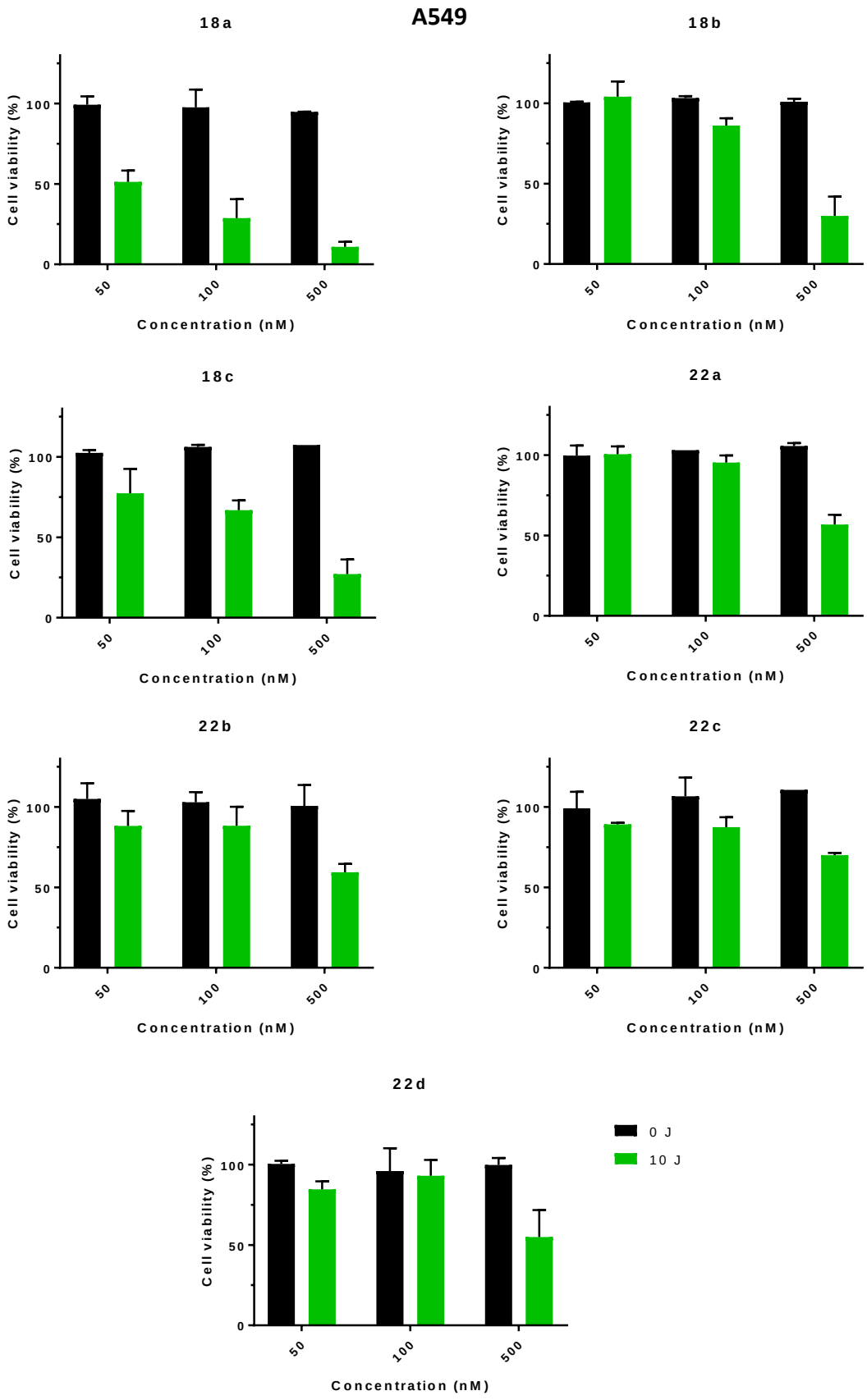

Figure 19: Cell viability of A549 cell line 24 hours after the photodynamic treatment (10 J) and without irradiation (0 J) based on three sensitizers concentrations. Results are presented as mean ± SD (at least n = 2).

Chapter 4: Conclusion and Future Perspectives

Throughout this dissertation the results obtained in the experimental work were presented and discussed. Still, there are important conclusions that need to be emphasized, as well as the prospect of future work.

The two-consecutive hetero-Diels-Alder reactions or conjugated additions of nitrosoalkenes with dipyrromethanes led to a new class of tetrapyrrolic compounds: bilanes *meso*-substituted with an oxime moiety. On-water reactions proved to be particularly interesting not only in the context of the development of a more sustainable methodology but because they are more than fifty times faster and can lead to different reactivities and selectivities in similar yields.

The oxidation of the bilanes gave *trans*-A_2B-corroles in satisfactory yields.

Corroles photophysical characterization revealed intense Q bands between 579 and 664 nm, values within the therapeutic window, and the absence of aggregation. These promising photophysical characteristics allow us to expect high photodynamic efficiency from the seven *trans*-A_2B-corroles studied.

Preliminary *in vitro* assays of corroles revealed high photocytotoxicity and non-cytotoxicity through MTT assays. The results obtained in the cell viability assays (SRB) corroborated to a large extent those obtained in the metabolic activity assays, which support its applicability as photosensitizers in PDT, pointing to a promising therapeutic effect, and support further studies.

In the future, it is planned to continue *in vitro* studies to assess the cytotoxicity of *trans*-A_2B-corroles in non-malignant cell lines of the lung, quantify the cellular uptake of the compounds in different cell lines (malignant and non-malignant), and evaluate the mechanism of cell death associated with these corroles. With these data, it will be possible to modify the structure of the corroles, in an attempt to further optimize photophysical characteristics and enhance their photodynamic efficiency, in order to validate the use of these compounds as photosensitizers in PDT.

Furthermore, it is planned to assess the potential anti-tumor effect of *trans*-A_2B-corroles *in vivo* in human tumor xenografts in mice. Here we hope to find results consistent with those obtained on *in vitro* assays, that the photosensitizers exhibit anti-tumor ability in the inhibition of lung tumor growth.

Chapter 5: References

1. Sudhakar, A. History of Cancer, Ancient and Modern Treatment Methods. *J. Cancer Sci. Ther.* **01**, i–iv (2009).
2. Laranjo, M. *Fotossensibilizadores Para Terapia e Imagem Em Oncologia*. (2014).
3. Smetana, K. *et al.* Ageing as an important risk factor for cancer. *Anticancer Research* **36**, 5009–5017 (2016).
4. Milanese, J.-S. & Wang, E. Germline mutations and their clinical applications in cancer. *Breast Cancer Manag.* **8**, BMT23 (2019).
5. Wild, C. P. *et al.* Cancer Prevention Europe. *Molecular Oncology* **13**, 528–534 (2019).
6. Stewart, B. W. & Wild, C. P. World cancer report 2014. *World Heal. Organ.* 1–2 (2014). doi:9283204298
7. Bray, F. *et al.* Global cancer statistics 2018: GLOBOCAN estimates of incidence and mortality worldwide for 36 cancers in 185 countries. *CA. Cancer J. Clin.* **68**, 394–424 (2018).
8. Teo, R. D., Hwang, J. Y., Termini, J., Gross, Z. & Gray, H. B. Fighting Cancer with Corroles. *Chem. Rev.* **117**, 2711–2729 (2017).
9. Siegel, R. L., Miller, K. D. & Jemal, A. Cancer statistics, 2020. *CA. Cancer J. Clin.* **70**, 7–30 (2020).
10. Cancer Today. Available at: https://gco.iarc.fr/today/online-analysis-map?v=2018&mode=cancer&mode_population=continents&population=900&populations=900&key=asr&sex=0&cancer=39&type=1&statistic=5&prevalence=0&population_group=0&ages_group%5B%5D=0&ages_group%5B%5D=17&nb_items=10&group_cancer=1&include_nmsc=1&include_nmsc_other=1&projection=natural-earth&color_palette=default&map_scale=quantile&map_nb_colors=5&continent=0&rotate=%255B10%252C0%255D. (Accessed: 6th August 2020)
11. Tsiouda, T. *et al.* Sex Differences and Adverse Effects between Chemotherapy and Immunotherapy for Non-Small Cell Lung Cancer. *J. Cancer* **11**, 3407–3415 (2020).
12. Lemjabbar-Alaoui, H., Hassan, O. U. I., Yang, Y. W. & Buchanan, P. Lung cancer: Biology and treatment options. *Biochimica et Biophysica Acta - Reviews on Cancer* **1856**, 189–210 (2015).
13. Surien, O., Ghazali, A. R. & Masre, S. F. Lung cancers and the roles of natural compounds as potential chemotherapeutic and chemopreventive agents. *Biomed. Pharmacol. J.* **12**, 85–98 (2019).
14. Campbell, J. D. *et al.* Distinct patterns of somatic genome alterations in lung adenocarcinomas and squamous cell carcinomas. *Nat. Genet.* **48**, 607–616 (2016).
15. Oser, M. G., Niederst, M. J., Sequist, L. V. & Engelman, J. A. Transformation from non-small-cell lung cancer to small-cell lung cancer: Molecular drivers and cells of origin. *The Lancet Oncology* **16**, e165–e172 (2015).

16. Zappa, C. & Mousa, S. A. Non-small cell lung cancer: Current treatment and future advances. *Transl. Lung Cancer Res.* **5**, 288–300 (2016).
17. Andreoli, T. E., Carpenter, C. C. J. & Cecil, R. L. *Andreoli and Carpenter's Cecil Essentials of Medicine - 9th Edition*. (Saunders, 2016).
18. David, A. R. & Zimmerman, M. R. Cancer: An old disease, a new disease or something in between? *Nature Reviews Cancer* **10**, 728–733 (2010).
19. Barreto, S., Barreto, M., Chaubal, R. & Dutt, A. The fight against cancer: Is it worthwhile? *Indian J. Med. Paediatr. Oncol.* **36**, 85–86 (2015).
20. Arruebo, M. *et al.* Assessment of the evolution of cancer treatment therapies. *Cancers* **3**, 3279–3330 (2011).
21. Quint, L. E. Lung cancer: Assessing resectability. *Cancer Imaging* **4**, 15–18 (2003).
22. Mokwena, M. G., Kruger, C. A., Ivan, M. T. & Heidi, A. A review of nanoparticle photosensitizer drug delivery uptake systems for photodynamic treatment of lung cancer. *Photodiagnosis and Photodynamic Therapy* **22**, 147–154 (2018).
23. Understanding Radiation Therapy | Cancer.Net. Available at: https://www.cancer.net/navigating-cancer-care/how-cancer-treated/radiation-therapy/understanding-radiation-therapy. (Accessed: 15th September 2020)
24. Shafirstein, G. *et al.* Photodynamic therapy of non-small cell lung cancer narrative review and future directions. *Annals of the American Thoracic Society* **13**, 265–275 (2016).
25. Jheon, S., Kim, T. & Kim, J. K. Photodynamic therapy as an adjunct to surgery or other treatments for squamous cell lung cancers. *Laser Ther.* **20**, 107–116 (2011).
26. Crous, A. & Abrahamse, H. Targeted Photodynamic Therapy for Improved Lung Cancer Treatment. in *Lung Cancer - Strategies for Diagnosis and Treatment* (InTech, 2018). doi:10.5772/intechopen.78699
27. Gorbe, M. *et al.* Synthesis and In Vitro Evaluation of a Photosensitizer-BODIPY Derivative for Potential Photodynamic Therapy Applications. *Chem. - An Asian J.* **10**, 2121–2125 (2015).
28. Agostinis, P. *et al.* Photodynamic therapy of cancer: An update. *CA. Cancer J. Clin.* **61**, 250–281 (2011).
29. Nascimento, B. F. O. *et al.* Ring-Fused Diphenylchlorins as Potent Photosensitizers for Photodynamic Therapy Applications: In Vitro Tumor Cell Biology and in Vivo Chick Embryo Chorioallantoic Membrane Studies. *ACS Omega* **4**, 17244–17250 (2019).
30. Dias-Ferreira, J. *et al.* Advances on photodynamic therapy through new pyridine-fused diphenylchlorins as photosensitizers for melanoma treatment. *Porto Biomed. J.* **2**, 227 (2017).
31. Dolmans, D. E. J. G. J., Fukumura, D. & Jain, R. K. Photodynamic therapy for cancer. *Nature Reviews Cancer* **3**, 380–387 (2003).
32. Dougherty, T. J. *et al.* Photodynamic therapy. *Journal of the National Cancer Institute* **90**, 889–905 (1998).
33. Mahammed, A. & Gross, Z. Corroles as triplet photosensitizers. *Coordination Chemistry*

Reviews **379**, 121–132 (2019).

34. Juarranz, Á., Jaén, P., Sanz-Rodríguez, F., Cuevas, J. & González, S. Photodynamic therapy of cancer. Basic principles and applications. *Clin. Transl. Oncol.* **10**, 148–154 (2008).
35. Shah, P. M. & Gerdes, H. Endoscopic options for early stage esophageal cancer. *Journal of Gastrointestinal Oncology* **6**, 20–30 (2015).
36. Nanashima, A. & Nagayasu, T. Current status of photodynamic therapy in digestive tract carcinoma in Japan. *International Journal of Molecular Sciences* **16**, 3434–3440 (2015).
37. Yano, T. *et al.* Phase I study of photodynamic therapy using talaporfin sodium and diode laser for local failure after chemoradiotherapy for esophageal cancer. *Radiat. Oncol.* **7**, (2012).
38. Yano, T. *et al.* Photodynamic therapy as salvage treatment for local failure after chemoradiotherapy in patients with esophageal squamous cell carcinoma: A phase II study. *Int. J. Cancer* **131**, 1228–1234 (2012).
39. Green, B., Cobb, A. R. M. & Hopper, C. Photodynamic therapy in the management of lesions of the head and neck. *Br. J. Oral Maxillofac. Surg.* **51**, 283–287 (2013).
40. Simone, C. B. & Cengel, K. A. Photodynamic therapy for lung cancer and malignant pleural mesothelioma. *Semin. Oncol.* **41**, 820–830 (2014).
41. Calixto, G., Bernegossi, J., de Freitas, L., Fontana, C. & Chorilli, M. Nanotechnology-Based Drug Delivery Systems for Photodynamic Therapy of Cancer: A Review. *Molecules* **21**, 342 (2016).
42. Kwiatkowski, S. *et al.* Photodynamic therapy – mechanisms, photosensitizers and combinations. *Biomedicine and Pharmacotherapy* **106**, 1098–1107 (2018).
43. Chatterjee, D. K., Fong, L. S. & Zhang, Y. Nanoparticles in photodynamic therapy: An emerging paradigm. *Advanced Drug Delivery Reviews* **60**, 1627–1637 (2008).
44. Allison, R. R. & Moghissi, K. Photodynamic Therapy (PDT): PDT Mechanisms. *Clin. Endosc.* **46**, 24 (2013).
45. Plaetzer, K., Krammer, B., Berlanda, J., Berr, F. & Kiesslich, T. Photophysics and photochemistry of photodynamic therapy: Fundamental aspects. *Lasers in Medical Science* **24**, 259–268 (2009).
46. Lucky, S. S., Soo, K. C. & Zhang, Y. Nanoparticles in photodynamic therapy. *Chemical Reviews* **115**, 1990–2042 (2015).
47. Castano, A. P., Demidova, T. N. & Hamblin, M. R. Mechanisms in photodynamic therapy: Part two - Cellular signaling, cell metabolism and modes of cell death. *Photodiagnosis and Photodynamic Therapy* **2**, 1–23 (2005).
48. Castano, A. P., Demidova, T. N. & Hamblin, M. R. Mechanisms in photodynamic therapy: Part three - Photosensitizer pharmacokinetics, biodistribution, tumor localization and modes of tumor destruction. *Photodiagnosis and Photodynamic Therapy* **2**, 91–106 (2005).
49. Josefsen, L. B. & Boyle, R. W. Unique diagnostic and therapeutic roles of porphyrins and

phthalocyanines in photodynamic therapy, imaging and theranostics. *Theranostics* **2**, 916–966 (2012).

50. O'Connor, A. E., Gallagher, W. M. & Byrne, A. T. Porphyrin and nonporphyrin photosensitizers in oncology: Preclinical and clinical advances in photodynamic therapy. *Photochemistry and Photobiology* **85**, 1053–1074 (2009).
51. Brandis, A. *et al.* Novel water-soluble bacteriochlorophyll derivatives for vascular-targeted photodynamic therapy: synthesis, solubility, phototoxicity, and the effect of serum proteins. *Photochem. Photobiol.* **81**, (2005).
52. Grabow, W. *METHOD FOR DETERMINATION OF SINGLET OXYGEN QUANTUM YIELDS FOR NEW FLUORENE-BASED PHOTOSENSITIZERS IN AQUEOUS MEDIA FOR THE ADVANCEMENT OF PHOTODYNAMIC THERAPY*. (2004).
53. Wall, K. P., Dillon, R. & Knowles, M. K. Fluorescence quantum yield measurements of fluorescent proteins: A laboratory experiment for a biochemistry or molecular biophysics laboratory course. *Biochem. Mol. Biol. Educ.* **43**, 52–59 (2015).
54. Benov, L. Photodynamic therapy: Current status and future directions. in *Medical Principles and Practice* **24**, 14–28 (S. Karger AG, 2015).
55. Celli, J. P. *et al.* Imaging and photodynamic therapy: Mechanisms, monitoring, and optimization. *Chem. Rev.* **110**, 2795–2838 (2010).
56. Albani, J. R. *Structure and Dynamics of Macromolecules: Absorption and Fluorescence Studies*. *Structure and Dynamics of Macromolecules: Absorption and Fluorescence Studies* (Elsevier, 2004). doi:10.1016/B978-0-444-51449-3.X5000-X
57. Joan Ribas Gispert. *Coordination Chemistry*. (2008).
58. Aguiar, M. A. de C. *Synthesis, photophysical characterization and biological evaluation of promising theranostic agents for cancer*. *Synthesis, photophysical characterization and biological evaluation of promising theranostic agents for cancer* (2018).
59. Plaetzer, K., Krammer, B., Berlanda, J., Berr, F. & Kiesslich, T. Photophysics and photochemistry of photodynamic therapy: Fundamental aspects. *Lasers in Medical Science* **24**, 259–268 (2009).
60. Martinez De Pinillos Bayona, A., Mroz, P., Thunshelle, C. & Hamblin, M. R. Design features for optimization of tetrapyrrole macrocycles as antimicrobial and anticancer photosensitizers. *Chemical Biology and Drug Design* **89**, 192–206 (2017).
61. Ochsner, M. Photophysical and photobiological processes in the photodynamic therapy of tumours. *J. Photochem. Photobiol. B Biol.* **39**, 1–18 (1997).
62. Foote, C. S. Definition of Type I and Type II Photosensitized Oxidation. *Photochem. Photobiol.* **54**, 659–659 (1991).
63. Redmond, R. W. & Kochevar, I. E. Spatially Resolved Cellular Responses to Singlet Oxygen. *Photochem. Photobiol.* **82**, 1178 (2006).
64. Collin, F. Chemical basis of reactive oxygen species reactivity and involvement in neurodegenerative diseases. *International Journal of Molecular Sciences* **20**, (2019).
65. Josefsen, L. B. & Boyle, R. W. Photodynamic Therapy and the Development of Metal-

Based Photosensitisers. *Met. Based. Drugs* **2008**, (2008).

66. Yano, S. *et al.* Current states and future views in photodynamic therapy. *Journal of Photochemistry and Photobiology C: Photochemistry Reviews* **12**, 46–67 (2011).
67. Ormond, A. B. & Freeman, H. S. Dye sensitizers for photodynamic therapy. *Materials* **6**, 817–840 (2013).
68. Lee, J. H. & Jung, M. Y. Direct Spectroscopic Observation of Singlet Oxygen Quenching and Kinetic Studies of Physical and Chemical Singlet Oxygen Quenching Rate Constants of Synthetic Antioxidants (BHA, BHT, and TBHQ) in Methanol. *J. Food Sci.* **75**, C506–C513 (2010).
69. Dąbrowski, J. M. Reactive Oxygen Species in Photodynamic Therapy: Mechanisms of Their Generation and Potentiation. in *Advances in Inorganic Chemistry* **70**, 343–394 (Academic Press Inc., 2017).
70. van Straten, D., Mashayekhi, V., de Bruijn, H. S., Oliveira, S. & Robinson, D. J. Oncologic photodynamic therapy: Basic principles, current clinical status and future directions. *Cancers* **9**, (2017).
71. Buytaert, E., Dewaele, M. & Agostinis, P. Molecular effectors of multiple cell death pathways initiated by photodynamic therapy. *Biochim. Biophys. Acta - Rev. Cancer* **1776**, 86–107 (2007).
72. Falk-Mahapatra, R. & Gollnick, S. O. Photodynamic Therapy and Immunity: An Update. *Photochem. Photobiol.* **96**, 550–559 (2020).
73. Kroemer, G. & Levine, B. Autophagic cell death: The story of a misnomer. *Nature Reviews Molecular Cell Biology* **9**, 1004–1010 (2008).
74. Mroz, P., Yaroslavsky, A., Kharkwal, G. B. & Hamblin, M. R. Cell death pathways in photodynamic therapy of cancer. *Cancers* **3**, 2516–2539 (2011).
75. Krammer, B. Vascular effects of photodynamic therapy. *Anticancer Research* **21**, 4271–4277 (2001).
76. Chen, B., Pogue, B. W., Hoopes, P. J. & Hasan, T. Vascular and cellular targeting for photodynamic therapy. *Critical Reviews in Eukaryotic Gene Expression* **16**, 279–306 (2006).
77. Brackett, C. M. & Gollnick, S. O. Photodynamic therapy enhancement of anti-tumor immunity. *Photochemical and Photobiological Sciences* **10**, 649–652 (2011).
78. Hunt, D. W. C. & Levy, J. G. Immunomodulatory aspects of photodynamic therapy. *Expert Opinion on Investigational Drugs* **7**, 57–64 (1998).
79. Castano, A. P., Mroz, P. & Hamblin, M. R. Photodynamic therapy and anti-tumour immunity. *Nature Reviews Cancer* **6**, 535–545 (2006).
80. Allison, R. R. & Moghissi, K. Photodynamic therapy (PDT): PDT mechanisms. *Clin. Endosc.* **46**, 24–29 (2013).
81. Kick, G., Messer, G., Goetz, A., Plewig, G. & Kind, P. Photodynamic therapy induces expression of interleukin 6 by activation of AP-1 but not NF-kappa B DNA binding. *Cancer Res.* **55**, 2373–9 (1995).

82. Castellino, F. & Germain, R. N. COOPERATION BETWEEN CD4 + AND CD8 + T CELLS: When, Where, and How . *Annu. Rev. Immunol.* **24**, 519–540 (2006).
83. Rocha, L. B., Gomes-Da-Silva, L. C., Dąbrowski, J. M. & Arnaut, L. G. Elimination of primary tumours and control of metastasis with rationally designed bacteriochlorin photodynamic therapy regimens. *Eur. J. Cancer* **51**, 1822–1830 (2015).
84. Gollnick, S. O., Vaughan, L. & Henderson, B. W. Generation of effective antitumor vaccines using photodynamic therapy. *Cancer Res.* **62**, 1604–1608 (2002).
85. Moghissi, K. Photodiagnosis and Photodynamic Therapy: The birth of a Journal. *Photodiagnosis and Photodynamic Therapy* **1**, 1 (2004).
86. Allison, R., Moghissi, K., Downie, G. & Dixon, K. Photodynamic therapy (PDT) for lung cancer. *Photodiagnosis and Photodynamic Therapy* **8**, 231–239 (2011).
87. Mroz, P., Hashmi, J. T., Huang, Y. Y., Lange, N. & Hamblin, M. R. Stimulation of anti-tumor immunity by photodynamic therapy. *Expert Review of Clinical Immunology* **7**, 75–91 (2011).
88. Dougherty, T. J. & Marcus, S. L. Photodynamic therapy. *Eur. J. Cancer* **28**, 1734–1742 (1992).
89. Jiang, X., Liu, R., Liu, H. & Chang, C. K. Corrole-based photodynamic antitumor therapy. *J. Chinese Chem. Soc.* **66**, 1090–1099 (2019).
90. Yoon, I., Li, J. Z. & Shim, Y. K. Advance in photosensitizers and light delivery for photodynamic therapy. *Clin. Endosc.* **46**, 7–23 (2013).
91. Kou, J., Dou, D. & Yang, L. Porphyrin photosensitizers in photodynamic therapy and its applications. *Oncotarget* **8**, 81591–81603 (2017).
92. Goslinski, T. & Piskorz, J. Fluorinated porphyrinoids and their biomedical applications. *Journal of Photochemistry and Photobiology C: Photochemistry Reviews* **12**, 304–321 (2011).
93. Szyszko, B., Biåek, M. J., Pacholska-Dudziak, E. & Latos-Grazyński, L. Flexible Porphyrinoids. *Chemical Reviews* **117**, 2839–2909 (2017).
94. Lopes, S. M. M., Pineiro, M. & Pinho e Melo, T. M. V. D. Corroles and Hexaphyrins: Synthesis and Application in Cancer Photodynamic Therapy. *Molecules* **25**, 3450 (2020).
95. Z, G., N, G. & I, S. The First Direct Synthesis of Corroles From Pyrrole. *Angew. Chem. Int. Ed. Engl.* **38**, (1999).
96. Lemon, C. M. Corrole photochemistry. *Pure Appl. Chem.* **0**, (2020).
97. You, L. *et al.* Photophysical properties of the Corrole photosensitizers. *Sci. China Physics, Mech. Astron.* **53**, 1491–1496 (2010).
98. Bevilacqua, A. C., Köhler, M. H. & Piquini, P. C. Corrole-Fullerene Dyads: Stability, Photophysical, and Redox Properties. *J. Phys. Chem. C* **123**, 20869–20876 (2019).
99. Alberto, M. E. *et al.* Iodine substituted phosphorus corrole complexes as possible photosensitizers in photodynamic therapy: Insights from theory. *J. Comput. Chem.* **41**, 1395–1401 (2020).
100. Zhao, F., Zhan, X., Lai, S. H., Zhang, L. & Liu, H. Y. Photophysical properties and singlet

oxygen generation of: Meso -iodinated free-base corroles. *RSC Adv.* **9**, 12626–12634 (2019).

101. Shao, W. *et al.* Photophysical properties and singlet oxygen generation of three sets of halogenated corroles. *J. Phys. Chem. B* **116**, 14228–14234 (2012).
102. Shi, L. *et al.* Fluorescence properties of halogenated mono-hydroxyl corroles: The heavy-atom effects. *J. Porphyr. Phthalocyanines* **13**, 1221–1226 (2009).
103. Hodgkinson, N., Kruger, C. A. & Abrahamse, H. Targeted photodynamic therapy as potential treatment modality for the eradication of colon cancer and colon cancer stem cells. *Tumour Biol.* **39**, 1010428317734691 (2017).
104. Barata, J. F. B. *et al.* Photodynamic effects induced by meso-tris(pentafluorophenyl)corrole and its cyclodextrin conjugates on cytoskeletal components of HeLa cells. *Eur. J. Med. Chem.* **92**, 135–144 (2015).
105. Cardote, T. A. F. *et al.* Pentafluorophenylcorrole-d-galactose conjugates. *Tetrahedron Lett.* **53**, 6388–6393 (2012).
106. Babu, B., Prinsloo, E., Mack, J. & Nyokong, T. Synthesis, characterization and photodynamic activity of Sn(iv) triarylcorroles with red-shifted Q bands. *New J. Chem.* **43**, 18805–18812 (2019).
107. Zhang, Z. *et al.* Synthesis, characterization and in vitro and in vivo photodynamic activities of a gallium(III) tris(ethoxycarbonyl)corrole. *Dalt. Trans.* **46**, 9481–9490 (2017).
108. Liang, Z. *et al.* Polyhydric Corrole and Its Gallium Complex: Synthesis, DNA-binding Properties and Photodynamic Activities. *Chinese J. Chem.* **34**, 997–1005 (2016).
109. Lim, P. *et al.* Differential cytostatic and cytotoxic action of metallocorroles against human cancer cells: Potential platforms for anticancer drug development. *Chem. Res. Toxicol.* **25**, 400–409 (2012).
110. Zhang, Z. *et al.* The photocytotoxicity effect of cationic sulfonated corrole towards lung cancer cells: in vitro and in vivo study. *Lasers Med. Sci.* **34**, 1353–1363 (2019).
111. Sun, Y. M. *et al.* DNA interaction and photodynamic antitumor activity of transition metal mono-hydroxyl corrole. *Bioorg. Chem.* **90**, (2019).
112. Cheng, F. *et al.* Photophysical properties and photodynamic anti-tumor activity of corrole-coumarin dyads. *J. Porphyr. Phthalocyanines* **22**, 886–898 (2018).
113. Wang, Y. G., Zhang, Z., Wang, H. & Liu, H. Y. Phosphorus(V) corrole: DNA binding, photonuclease activity and cytotoxicity toward tumor cells. *Bioorg. Chem.* **67**, 57–63 (2016).
114. Huang, Z. *et al.* Photodynamic therapy for treatment of solid tumors - Potential and technical challenges. *Technology in Cancer Research and Treatment* **7**, 309–320 (2008).
115. Mallidi, S. *et al.* Beyond the barriers of light penetration: Strategies, perspectives and possibilities for photodynamic therapy. *Theranostics* **6**, 2458–2487 (2016).
116. Lopes, S. M. M. & Pinho E Melo, T. M. V. D. Meso-Substituted Corroles from Nitrosoalkenes and Dipyrromethanes. *J. Org. Chem.* **85**, 3328–3335 (2020).
117. Yokoyama, M. & Takeshima, T. Chemistry of β-iminosulfoxide. Ketone from β-

iminosulfoxide. *Tetrahedron Lett.* **19**, 147–150 (1978).

118. Kim, K., Cho, J. & Yoon, S. C. Reactions of tetrasulfur tetranitride with aryl dibromomethyl ketones: One-pot synthesis of 3-aroylformamido-4-aryl-1,2,5-thiadiazoles and their reactions. *J. Chem. Soc. Perkin Trans. 1* 253–259 (1995). doi:10.1039/p19950000253
119. Yoon, S. C., Cho, J. & Kim, K. Reactions of 1-aryl-2,2-dihalogenoethanone oximes with tetrasulfur tetranitride (S4N4): A general method for the synthesis of 3-aryl-4-halogeno-1,2,5-thiadiazoles. *J. Chem. Soc. - Perkin Trans. 1* 109–116 (1998). doi:10.1039/a704408i
120. Benjamin J. Littler *et al.* Refined Synthesis of 5-Substituted Dipyrromethanes. (1999). doi:10.1021/JO982015+
121. Sarma, K. D., Ray, D. & Antony, A. Improved sensitivity of trypan blue dye exclusion assay with Ni2+ or Co2+ salts. *Cytotechnology* **32**, 93–95 (2000).
122. Mosmann, T. Rapid colorimetric assay for cellular growth and survival: Application to proliferation and cytotoxicity assays. *J. Immunol. Methods* **65**, 55–63 (1983).
123. Papazisis, K. T., Geromichalos, G. D., Dimitriadis, K. A. & Kortsaris, A. H. Optimization of the sulforhodamine B colorimetric assay. *J. Immunol. Methods* **208**, 151–158 (1997).
124. Vichai, V. & Kirtikara, K. Sulforhodamine B colorimetric assay for cytotoxicity screening. *Nat. Protoc.* **1**, 1112–1116 (2006).
125. Lopes, S. M. M., Cardoso, A. L., Lemos, A. & Pinho e Melo, T. M. V. D. Recent Advances in the Chemistry of Conjugated Nitrosoalkenes and Azoalkenes. *Chem. Rev.* **118**, 11324–11352 (2018).
126. Pereira, N., Lopes, S., Lemos, A. & Pinho e Melo, T. On-Water Synthesis of Dipyrromethanes via Bis-Hetero-Diels–Alder Reaction of Azo- and Nitrosoalkenes with Pyrrole. *Synlett* **25**, 423–427 (2013).
127. Nunes, S. C. C. *et al.* Reactions of nitrosoalkenes with dipyrromethanes and pyrroles: Insight into the mechanistic pathway. *J. Org. Chem.* **79**, 10456–10465 (2014).
128. De Los Santos, J. M., Rubiales, G., Sbai, Z. E., Ochoa de Retana, A. M. & Palacios, F. Reaction of phosphinylated nitrosoalkenes with electron-rich heterocycles. Electrophilic aromatic substitution vs. cycloaddition. *Org. Biomol. Chem.* **15**, 662–671 (2017).
129. Gouterman, M. Study of the effects of substitution on the absorption spectra of porphin. *J. Chem. Phys.* **30**, 1139–1161 (1959).
130. Gouterman, M. Spectra of porphyrins. *J. Mol. Spectrosc.* **6**, 138–163 (1961).
131. Mosmann, T. Rapid colorimetric assay for cellular growth and survival: Application to proliferation and cytotoxicity assays. *J. Immunol. Methods* **65**, 55–63 (1983).
132. Vistica, D. T. *et al.* Tetrazolium-based Assays for Cellular Viability: A Critical Examination of Selected Parameters Affecting Formazan Production. *Cancer Res.* **51**, (1991).

List of figures

List of tables